Published in final edited form as:
Nature. 2016 August 25; 536(7617): 431–436. doi:10.1038/nature19083.

Molecular basis of APC/C regulation by the spindle assembly checkpoint

Claudio Alfieri[#1], **Leifu Chang**[#1], **Ziguo Zhang**[1], **Jing Yang**[1], **Sarah Maslen**[1], **Mark Skehel**[1], and **David Barford**[1]

[1]MRC Laboratory of Molecular Biology, Francis Crick Avenue, Cambridge, CB2 0QH, UK

[#] These authors contributed equally to this work.

Abstract

In the dividing eukaryotic cell the spindle assembly checkpoint (SAC) ensures each daughter cell inherits an identical set of chromosomes. The SAC coordinates the correct attachment of sister chromatid kinetochores to the mitotic spindle with activation of the anaphase-promoting complex/cyclosome (APC/C), the E3 ubiquitin ligase that initiates chromosome separation. In response to unattached kinetochores, the SAC generates the mitotic checkpoint complex (MCC), a multimeric assembly that inhibits the APC/C, delaying chromosome segregation. Here, using cryo-electron microscopy we determined the near-atomic resolution structure of an APC/C-MCC complex (APC/C^{MCC}). We reveal how degron-like sequences of the MCC subunit BubR1 block degron recognition sites on Cdc20, the APC/C coactivator subunit ($Cdc20^{APC/C}$) responsible for substrate interactions. BubR1 also obstructs binding of UbcH10 (APC/C's initiating E2) to repress APC/C ubiquitination activity. Conformational variability of the complex allows for UbcH10 association, and we show from a structure of APC/C^{MCC} in complex with UbcH10 how the Cdc20 subunit intrinsic to the MCC ($Cdc20^{MCC}$) is ubiquitinated, a process that results in APC/C reactivation when the SAC is silenced.

The fidelity of chromosome separation at each cell division cycle ensures the inheritance of the correct complement of genetic material in successive generations of cells. The APC/C initiates sister chromatid separation by controlling the proteasomal degradation of securin and cyclin B 1,2. Their degradation allows separase to remove sister chromatid cohesin. Critical to the maintenance of chromosome integrity of dividing cells is the SAC 3,4. The

Correspondence should be addressed to D.B. (dbarford@mrc-lmb.cam.ac.uk).

Author contributions. Z.Z. cloned an initial mutant MCC construct used by C.A. to generate other MCC constructs. C.A. cloned Cdc20, purified proteins, performed the protein complex reconstitutions and biochemical analysis. C.A. and L.C. prepared grids, collected and analysed EM data and determined the 3D reconstructions. C.A. fitted coordinates, built models and made the figures with help of L.C. Z.Z. together with J.Y. generated APC/C viruses. J.Y. provided E1, E2 and ubiquitin for ubiquitination assays. S.M. and M.S. performed mass spectrometry. D.B. directed the project and designed experiments with C.A. C.A. and D.B. wrote the manuscript.

Author information. EM maps are deposited with EM-DB with accession code EMD-4037. Protein coordinates of APC/C^{MCC} are deposited with RCSB with PDB code 5LCW.

The authors declare no competing financial interests.

Europe PMC Funders Author Manuscripts

SAC responds to unattached kinetochores by generating the MCC which functions to suppress APC/C-catalysed ubiquitination of securin and cyclin B.

Although the components of the SAC machinery are known 5,6, and some details of the molecular events that sense the absence of kinetochore attachment (and possibly intra-kinetochore tension) to signal MCC assembly have been characterized, important questions remain 4. Intrinsic to this process is the conversion of O-Mad2 to C-Mad2 catalysed by a C-Mad2-Mad1 complex at unattached kinetochores 7–9. Soluble C-Mad2 engages the N-terminus of Cdc20 (refs 10,11), the mitotic activating subunit of the APC/C, which then binds the BubR1-Bub3 dimer to form the MCC 12. Mad2 and BubR1 interact cooperatively with Cdc20 (refs 9,13–18), and synergistically inhibit the APC/C in mitosis 14,19.

In an important advance, it was proposed 2, and shown 20, that the tetrameric MCC inhibits the APC/C already in complex with Cdc20 (the regulatory subunit that recognizes D box, KEN box and ABBA motif degrons of APC/C substrates and that promotes the catalytically active conformation of the APC/C [APC/C^{Cdc20}]) 21,22. In addition to inhibiting the APC/C, the MCC contributes to APC/C reactivation after SAC silencing through proteasome-catalysed Cdc20 degradation 23,24. SAC-mediated Cdc20 proteolysis is APC/C, Mad2 and BubR1/Mad3-dependent 17,23–27, suggesting that Cdc20 ubiquitination occurs in the context of the APC/C^{MCC}, an idea supported by findings that release from mitotic arrest, concomitant with Cdc20 destruction, requires the small APC/C subunit Apc15 (refs 28–30).

To obtain insights into reciprocal APC/C and MCC regulation, we reconstituted recombinant APC/C^{MCC} and APC/C^{MCC} with UbcH10 (APC/C's initiating E2) complexes for structural and biochemical analysis. From a cryo-EM reconstruction of the APC/C^{MCC}, we identify conformational variability of the complex that explains its capacity to repress substrate ubiquitination, but also allows for UbcH10 to catalyse intramolecular $Cdc20^{MCC}$ ubiquitination.

Reconstitution and overall features of APC/C^{MCC}

We reconstituted recombinant APC/C^{MCC} using the insect cell/baculovirus expression system. Recombinant APC/C^{MCC} incorporates two distinct Cdc20 subunits, termed $Cdc20^{APC/C}$ for the APC/C^{Cdc20}-associated subunit, and $Cdc20^{MCC}$ for the MCC-associated subunit (Extended Data Fig. 1a, j and Extended Data Table 1), consistent with 2,20. We determined negative stain and cryo-EM reconstructions of the APC/C^{MCC} complex (Extended Data Table 2). The negative stain EM reconstruction of the recombinant APC/C^{MCC} is essentially identical in structure to endogenous APC/C^{MCC} isolated from checkpoint-arrested HeLa cells determined at a similar resolution 31 (Extended Data Fig. 2b). This substantiates the model that the physiological form of APC/C^{MCC} includes two Cdc20 subunits 2,20. Both reconstructions feature a large density element termed the MCC-$Cdc20^{APC/C}$ module (MCC interacting with the $Cdc20^{APC/C}$ subunit of APC/C^{Cdc20}) occupying APC/C's central cavity, extending from the "front" side of the platform domain (Extended Data Fig. 2b).

To understand quantitatively how the MCC interacts with APC/C^{Cdc20}, we determined a cryo-EM reconstruction of APC/C^{MCC} at near-atomic resolution (Fig. 1a, b and Extended Data Figs 2c-e and 3 and Extended Data Table 2). Extensive 3D classification of APC/C^{MCC} revealed conformational variability of the MCC-$Cdc20^{APC/C}$ module. This module adopts a stable rigid conformation in 21% of APC/C^{MCC} particles (defined as APC/$C^{MCC\text{-}Closed}$) (Extended Data Fig. 4b, class 1). A local resolution map of APC/$C^{MCC\text{-}Closed}$ shows that the central rigid regions are at 3.9 to 4.1 Å resolution, with the flexible outer regions at lower resolution (Extended Data Fig. 3c, d). We built an atomic model of APC/$C^{MCC\text{-}Closed}$ (Fig. 1 and Supplementary Video 1) guided by the cryo-EM structure of human APC/$C^{Cdh1.Emi1}$ (ref. 32) and the crystal structure of fission yeast MCC 18.

In the APC/$C^{MCC\text{-}Closed}$ reconstruction, the secondary structure elements of the MCC-$Cdc20^{APC/C}$ module are clearly visible (Extended Data Fig. 2e), revealing that $Cdc20^{APC/C}$, $Cdc20^{MCC}$, Mad2 and the N-terminal and middle regions of BubR1, including its tetratricopeptide (TPR) domain (BubR1^{TPR}) and its inhibitory degrons, are well defined (Figs 1a, b and 2a). However, despite their presence in reconstituted APC/C^{MCC} (Extended Data Figs 1a and 2a), the C-terminal pseudo-kinase domain of BubR1 (Fig. 2a) and Bub3, were not visible in EM density, indicative of conformational variability. In agreement with this, both the structure and activity of APC/C^{MCC} with Bub3 and the BubR1 C-terminus deleted (APC/$C^{miniMCC}$) are indistinguishable from APC/C^{MCC} (Extended Data Figs 1b, h, i and 2b). These data are consistent with the requirement of BubR1's N-terminal ~363 residues (Fig. 2a) to sustain a SAC 33–36.

General architecture of APC/C^{MCC}

In APC/C^{MCC}, the MCC core elements comprising $Cdc20^{MCC}$, BubR1^{TPR}, and Mad2 resemble their counterparts in *S. pombe* MCC 18 (Fig. 1 and Supplementary Video 1). Mad2 adopts the closed conformation (C-Mad2) with its C-terminal segment ('safety belt') locking the tubular density of the $Cdc20^{MCC}$ KILR motif 10,11 (Figs 1 and 2c and Extended Data Fig. 5c). The MCC docks into the APC/C^{Cdc20} cavity directly below $Cdc20^{APC/C}$ and interacts with $Cdc20^{APC/C}$ such that the two Cdc20 WD40 domains of APC/C^{MCC} are arranged in an almost perpendicular fashion (Figs 1 and 2c). $Cdc20^{MCC}$ and BubR1 mediate interactions between the MCC and APC/C^{Cdc20}, with BubR1 dominating these interactions through its contacts to $Cdc20^{APC/C}$ and Apc2. C-Mad2 forms no direct contacts to APC/C^{Cdc20} (Fig. 1). However, by stabilizing BubR1's association with $Cdc20^{MCC}$, C-Mad2 indirectly augments BubR1 interactions with APC/C^{Cdc20} (refs 14,19,35). APC/$C^{MCC\text{-}Closed}$ is similar in structure to APC/C-coactivator complexes 22,32, with major conformational differences confined to $Cdc20^{APC/C}$ and the platform subunits Apc4, Apc5 and Apc15 (Extended Data Fig. 5d, e).

Contacts between the two Cdc20 subunits of APC/$C^{MCC\text{-}Closed}$ are mainly mediated by BubR1 that intertwines between them (Fig. 2c). In response to MCC binding, the WD40 domain of $Cdc20^{APC/C}$ is tilted by ~40° and rotated 90° about its central axis (Extended Data Fig. 5d) 22. This disrupts the D box-binding site formed by the interface of the D box co-receptors of $Cdc20^{APC/C\text{-}WD40}$ and Apc10 (refs 21,32), and pulls the C-terminal IR tail of APC/C^{Cdc20} away from the IR-tail binding site of Apc3A. A disengagement of the

Cdc20$^{APC/C}$ IR tail from Apc3A is consistent with weak EM density at the IR tail-binding site (Extended Data Fig. 5a), and the finding that Cdc20 does not require Apc3 to bind the APC/C when the SAC is active 37. In contrast to the IR tail, the N-terminal domain of Cdc20$^{APC/C}$ maintains the same interactions with Apc8B and Apc1^{PC} as seen in APC/C^{Cdc20} (ref. 22) (Fig. 3a and Extended Data Fig. 5b).

Degron motifs of BubR1 interact with both Cdc20 subunits of APC/C^{MCC}

Similar to yeast MCC 18, in APC/C^{MCC}, the N-terminal KEN-1 box (K1) (Fig. 2a and Supplementary Video 1), engages the KEN box-recognition site of the Cdc20^{MCC} (Fig. 2b, c). Immediately following BubR1^{TPR} and preceding KEN-2 (K2) is the N-terminal D box motif (D1) 20 (Fig. 2a). We assigned D1 to the loop-like density at the D-box recognition site of Cdc20$^{APC/C}$, although due to the re-orientation of Cdc20$^{APC/C}$ in APC/C^{MCC}, its position is diametrically opposed to its location in active APC/C-coactivator complexes (Extended Data Fig. 5d) 21,22,32. D1 and its flanking residues mediate the interface of Cdc20$^{APC/C}$ and Cdc20^{MCC} (Figs 1 and 2c lower panel). This explains how mutating D1 disrupts MCC binding to a second Cdc20 subunit without affecting MCC integrity 20. By engaging the Cdc20$^{APC/C}$ D-box co-receptor in APC/C^{MCC}, D1 would obstruct D box-dependent substrate recognition, consistent with its requirement for a checkpoint arrest 20.

EM density immediately C-terminal to D1 is disordered (Fig. 2c, lower panel) however, uninterrupted tubular density situated nearby and assigned to BubR1 is clearly defined wrapping around the opposite side of the Cdc20$^{APC/C}$ WD40 domain, connecting its bottom and top surfaces and contacting both the Cdc20$^{APC/C}$ KEN and ABBA motif-binding sites (labelled A1 and K2 in Fig. 2c). This BubR1-EM density feature bears a striking resemblance to the structure of Acm1 (APC/C-Cdh1-modulator 1), an inhibitor of yeast Cdh1 that utilizes ABBA, D box and KEN motifs to block the degron-recognition sites of Cdh1 (ref. 38) (Extended Data Fig. 6a). The BubR1 EM density contacting the top surface of Cdc20$^{APC/C}$ corresponds to the KEN-2 box (K2) (Fig. 2c, top panel). Guided by the Cdh1-Acm1 crystal structure 38, we modelled the KEN-2 box and the preceding ABBA motif (A1) (Fig. 2a and Extended Data Fig. 6a-c), to the KEN box and ABBA motif recognition sites of Cdc20$^{APC/C}$ (Fig. 2c).

The KEN-2 motif is invariant in BubR1 orthologs (Extended Data Fig. 6b), and although not required for MCC assembly 16,18,20,26,36,39, is essential for a spindle checkpoint arrest 16,26,36,39. Thus, similar to D1, a role for KEN-2 in mediating MCC interactions with APC/C^{Cdc20} would explain its requirement in the SAC through stabilizing MCC interactions with Cdc20$^{APC/C}$ (ref. 20) and inhibiting degron recognition by APC/C^{Cdc20}.

A middle segment of metazoan BubR1 includes an ABBA motif and a D box (A2 and D2, respectively) (Fig. 2a) that mediate Cdc20-BubR1 interactions in a Mad2-independent manner 15,19,40–43. These motifs contribute weakly to sustaining the SAC 15,41,42, and play a role to recruit Cdc20 to unattached kinetochores 40–42. The tubular EM densities located at the ABBA motif and D-box recognition sites of Cdc20^{MCC} were assigned to these motifs (Fig. 2c, top panel).

Cdc20^{MCC} contacts to the APC/C

Although Cdc20^{MCC} interactions with the APC/C are mainly mediated through BubR1 and APC/C^{Cdc20}, two additional contacts are notable. First, the C-terminal IR tail of Cdc20^{MCC} binds to a site on Apc8A that is structurally equivalent to the Cdc20$^{APC/C}$ C-box binding site on Apc8B 32 (Fig. 3a and Supplementary Video 1). This interaction can be rationalized from the similarities in how the Apc3-IR tail and Apc8-C box binding sites interact with their cognate IR tail and C box motifs, respectively 32. Second, the lower surface of the Cdc20^{MCC} WD40 domain interacts with the conserved acidic region of the Apc4 helix-bundle domain (Apc4^{HBD}), close to the UbcH10 binding site 32,44 (Figs 2c and 3a, b).

The MCC suppresses APC/C E3 ligase activity

UbcH10 interacts with the APC/C through the RING domain of Apc11 and the winged-helix B (WHB) domain of Apc2 (Apc2^{WHB}) 32,44. In APC/C$^{MCC\text{-}Closed}$, BubR1^{TPR} occludes both E2-binding sites (Figs 1 and 3). BubR1^{TPR} interacts directly with the UbcH10 interface of Apc2^{WHB} that repositions to contact BubR1^{TPR} (Fig. 3b-d and Extended Data Figs 5g and 6c) 32,44. Thus, in APC/C$^{MCC\text{-}Closed}$, the steric occlusion of UbcH10 binding would inhibit ubiquitin chain synthesis.

Apc15-dependent conformational flexibility of the MCC

The APC/C$^{MCC\text{-}Closed}$ structure explains how the MCC inhibits APC/C^{Cdc20} through obstructing substrate and UbcH10 interactions. However, Cdc20 auto-ubiquitination is the trigger for the spontaneous reactivation of the APC/C 23–29,45, dependent on the small APC/C subunit Apc15 (refs 28,29). In previously reported APC/C structures 22,32, Apc15 adopts an extended conformation, anchored to Apc5 by its N-terminus, and bridging Apc5 and Apc8A through its adjacent N-terminal helix (Apc15^{NTH}). Strikingly, in APC/C$^{MCC\text{-}Closed}$, Apc15^{NTH} is structurally disordered. This results from Cdc20^{MCC} shifting the tip of Apc4^{HBD} that concomitantly repositions the adjacent N-terminal domain of Apc5 (Apc5^{NTD}), disrupting its interaction with Apc15^{NTH} (Fig. 4a, b and Extended Data Fig. 5d, e and Supplementary Video 2). The disorder of Apc15^{NTH} and repositioning of Apc4^{HBD} and Apc5^{NTD} in APC/C$^{MCC\text{-}Closed}$ contrasts to their conformations in another structural state representing only 2% of APC/C^{MCC} particles (termed APC/C$^{MCC\text{-}Open}$) (Methods and Extended Data Fig. 4a, b and Extended Data Table 2). In APC/C$^{MCC\text{-}Open}$, EM density assigned to the MCC-Cdc20$^{APC/C}$ module is weaker relative to APC/C$^{MCC\text{-}Closed}$. However, EM density for Apc15^{NTH} is clearly defined (Fig. 4e, f). Moreover, in APC/C$^{MCC\text{-}Open}$, MCC-Cdc20$^{APC/C}$ is shifted towards APC/C's TPR lobe, disrupting contacts between the MCC and the catalytic module, Apc4^{HBD} and Apc10. The 'open' position of MCC-Cdc20$^{APC/C}$ is stabilized by Apc15^{NTH} interacting with Apc5^{NTD} that pushes onto the Cdc20^{MCC}-binding site of Apc4^{HBD} (Fig. 4f and Extended Data Fig. 5e). Thus, the stability of Apc15^{NTH} influences the transition between open and closed conformations of the MCC-Cdc20$^{APC/C}$ module.

To further investigate how Apc15 modulates the position of MCC-Cdc20$^{APC/C}$, we determined the structure of APC/C^{MCC} with Apc15 deleted (APC/C$^{\Delta Apc15}$) (Extended Data

Table 2 and Fig. 4c, d and Extended Data Fig. 3). APC/$C^{\Delta Apc15}$ assembled similarly to wild type APC/C and was catalytically active towards securin (Extended Data Fig. 1k-l). However, in contrast to APC/C^{MCC}, the reconstituted APC/$C^{\Delta Apc15\text{-}MCC}$ was defective for Cdc20 auto-ubiquitination, consistent with 28,29 (Fig. 5c and Extended Data Fig. 1h). 3D classification of the APC/$C^{\Delta Apc15\text{-}MCC}$ cryo-EM data set showed that the MCC-$Cdc20^{APC/C}$ module adopts only the closed configuration (Fig. 4c, d and Extended Data Fig. 7b and Supplementary Video 2), with no evidence of APC/$C^{MCC\text{-}Open}$ (Extended Data Fig. 7a, classes 1 to 6). Thus, the absence of Apc15 promotes APC/$C^{MCC\text{-}Closed}$, explaining why Apc15 is necessary for Cdc20 ubiquitination. In support of our structural data that $Apc15^{NTH}$ is required to stabilize APC/$C^{MCC\text{-}Open}$, similar to APC/$C^{\Delta Apc15\text{-}MCC}$, APC/$C^{MCC}$ reconstituted with Apc15 lacking the $Apc15^{NTH}$ ($Apc15^{\Delta NTH}$), is defective in Cdc20 auto-ubiquitination (Fig. 5e, lanes 8 & 9 and Extended Data Fig. 1h).

Since interactions between $Apc2^{WHB}$ and BubR1 stabilize APC/$C^{MCC\text{-}Closed}$ (Figs 1 and 3b), disrupting this interface should favour APC/$C^{MCC\text{-}Open}$. Consistent with this idea, negative stain EM reconstructions of an APC/C^{MCC} mutant with $Apc2^{WHB}$ deleted showed APC/C^{MCC} adopting the open conformation, with no APC/$C^{MCC\text{-}Closed}$ (Extended Data Figs 1c and 2b). Importantly, in the complementary $Apc2^{WHB}$-binding surface mutant of BubR1 (Extended Data Fig. 5g), $Cdc20^{MCC}$ auto-ubiquitination is stimulated ($BubR1^{Wm}$, Fig. 5d and Extended Data Fig. 1h).

Mechanism of $Cdc20^{MCC}$ auto-ubiquitination from an APC/$C^{UbcH10\text{-}MCC}$ structure

$Cdc20^{MCC}$ auto-ubiquitination catalysed by APC/C^{MCC}-UbcH10 is an intra-molecular process reliant on the APC/$C^{MCC\text{-}Open}$ conformation. To further explore this possibility, we determined the cryo-EM structure of APC/C^{MCC} in complex with UbcH10 (APC/$C^{UbcH10\text{-}MCC}$) (Extended Data Table 2). A 3D reconstruction using 7% of total particles showed clear EM density for both UbcH10 and the MCC-$Cdc20^{APC/C}$ module (Extended Data Fig. 7c). The the resultant EM map at 8.9 Å resolution allowed rigid body docking of the APC/C, UbcH10 and MCC-$Cdc20^{APC/C}$ coordinates. APC/$C^{UbcH10\text{-}MCC}$ resembles APC/$C^{MCC\text{-}Open}$ (Figs 4e-h and 5a and Extended Data Fig. 3 and Supplementary Video 2). $Apc15^{NTH}$ is ordered and MCC-$Cdc20^{APC/C}$ is rotated towards the TPR lobe leaving the catalytic module accessible to bind UbcH10 (Fig. 5a).

Strikingly, in APC/$C^{UbcH10\text{-}MCC}$, UbcH10 induces an additional small rotation of MCC-$Cdc20^{APC/C}$. The C-terminus of $Cdc20^{MCC}$ is visualized as an extended tubular density feature linking the $Cdc20^{MCC}$ WD40 domain with the catalytic site of UbcH10 (Fig. 5b & Extended Data Fig. 3e and Supplementary Video 2). Modelling the C-terminus of $Cdc20^{MCC}$ into this density shows that Lys485 and Lys490 are accessible to the UbcH10 catalytic site (Fig. 5b). Both residues are ubiquitinated *in vitro* (data not shown), and their replacement by Arg virtually eliminated Cdc20 auto-ubiquitination (Fig. 5e), indicating that these two residues are the major sites of $Cdc20^{MCC}$ ubiquitination in the context of APC/$C^{MCC\text{-}UbcH10}$. Our model that the MCC competitively restricts access of UbcH10 to its binding site on the APC/C is consistent with the reduced binding of UbcH10 to endogenous

APC/C^{MCC} relative to APC/C^{Cdc20} (ref. 31), and our finding that compared with securin ubiquitination, Cdc20 auto-ubiquitination required a 10-fold higher concentration of UbcH10 (Extended Data Fig. 1m), in agreement with 29. Although our data show that MCC suppresses APC/C - UbcH10 interactions, the effect of the MCC on modulating the affinity of the APC/C for the elongating E2 Ube2S, which contributes to checkpoint silencing 46–48, is less clear. The binding site for the Ube2S C-terminal LR tail at the Apc2-Apc4 interface 32, necessary for its association with the APC/C, is unaffected by the MCC (Fig. 5a), thus in principle allowing Ube2S to assemble ubiquitin chains onto the C-terminus of $Cdc20^{MCC}$. However, the capacity of Cdc20 to stabilize APC/C – Ube2S complexes 48, may be affected by the interactions of BubR1 with the APC/C^{MCC}.

In conclusion, our structural analysis of APC/C^{MCC} and APC/$C^{UbcH10\text{-}MCC}$ provides a molecular explanation for the spontaneous APC/C reactivation resulting from SAC inactivation involving ubiquitin-mediated $Cdc20^{MCC}$ proteolysis. APC/C reactivation in response to the cessation of SAC signalling is facilitated by the reciprocal control of APC/C and MCC activities mediated by the conformational flexibility of APC/C^{MCC}, influenced by Apc15. Modulation of this conformational change could allow for the regulation of $Cdc20^{MCC}$ auto-ubiquitination (Fig. 5f). A candidate for such a role is $p31^{comet}$, a Mad2-binding protein proposed to stimulate Cdc20 ubiquitination in checkpoint-arrested cells 23,45.

Methods

Cloning and expression of human APC/C complex genes

The DNA coding sequences (CDSs) of the human APC/C subunits (wild type, mutant $Apc2^{\Delta WHB}$, Apc11-UbcH10 fusion and ΔApc15 were assembled by USER cloning into a modified version of the insect cell-baculovirus MultiBac expression system 32,51,52. All APC/C subunit CDSs were distributed in two recombinant vectors that were used for recombinant baculovirus generation. For APC/C expression, Hi-5 cells at a density of $2x10^6$ cells/mL were co-infected with two pre-cultures of Sf9 cells each pre-infected with one of the two recombinant APC/C baculoviruses. APC/C expression (unphosphorylated) was performed for 30 h. To obtain APC/C^{OA} (phosphorylated APC/C), okadaic acid at a final concentration of 0.1 μM was added after 24 h of infection. Cells were harvested after 5 h of treatment.

Cloning and expression of human MCC complex genes and Cdc20

The CDSs of the human MCC subunits (Mad2, Cdc20, BubR1, Bub3) used for structural analysis were cloned into a pU2 plasmid 52 using the same method as for the APC/C. BubR1 was fused in frame with an N-terminal 3xFLAG tag. Cdc20 for individual expression was cloned into a pFastbac1HTA in frame with the His_6-tag. In addition, an MBP tag followed by a TEV site between the starting codon of Cdc20 and the N-terminal His_6 tag was added by restriction free cloning method (RF-cloning 53). To obtain a vector containing Mad2, Cdc20 and BubR1 (residues 1-569) CDSs (miniMCC construct), a Mad2 and Cdc20-containing expression cassette from a pU1 vector was shuttled (by the AvrII and PmeI sites) into a pFastbacDual vector (BstZ171 and SpeI sites) that contained 3xFLAG-$BubR1^{1\text{-}569}$

under the control of the p10 promoter. A C-terminal StrepIIx2 tag was added by RF-cloning into the BubR1 constructs used in ubiquitination assays. Expression of either the MCC or Cdc20 constructs was performed similarly to the APC/C (unphosphorylated) to avoid CDK-dependent inhibition of APC/C-Cdc20 interactions 54,55. Moreover, cells were harvested 48 h after infection. To express MCC complexes with the tagged versions of BubR1, virus containing the BubR1-StrepII constructs was co-infected with MCC virus. To express the MCC complex with the $Cdc20^{K485R,R490R}$ mutations, viruses containing the individual MCC subunits were used for co-infection. $Apc15^{\Delta NTH}$, a mutant form of Apc15 with a $(Gly\text{-}Ser\text{-}Ala)_6$ linker substitution of the N-terminal helix (NTH: residues 23-57) was cloned into an *E. coli* pOPIN expression vector and purified using a C-terminal $StrepII^{x2}$ tag.

Reconstitution and purification of APC^{MCC} complexes

To generate mitotic phosphorylated APC/C (APC/C^{OA}) we incubated APC/C expressing insect cells with the phosphatase inhibitor okadaic acid (OA) (as described above). The extent of APC/C phosphorylation was monitored by assessing the migration of the Apc3 subunit on SDS PAGE 56 (Extended Data Fig. 1a, f). The recombinant APC/C^{OA} was phosphorylated on ~110 sites (Extended Data Table 3), correlating closely with those previously identified in endogenous APC/C isolated from HeLa cells arrested by the mitotic checkpoint 56–58, and with sites phosphorylated *in vitro* by the mitotic APC/C activating kinases Cdk2-cyclinA2-Cks2 and Plk1 (ref. 22 (Extended Data Table 3). Compared with APC/C from untreated insect cells, and using Cdc20 as the coactivator, APC/C^{OA} readily ubiquitinates securin (Extended Data Fig. 1g, h).

The APC/C^{MCC} complex was reconstituted by co-lysing APC/C^{OA} expressing cells with insect cells expressing separately MBP-tagged Cdc20 and the MCC (BubR1, Bub3, Mad2 and untagged Cdc20). Hi-5 cell pellets expressing either APC/C^{OA} or MBP-Cdc20 or MCC were mixed together in reconstitution buffer containing 50 mM Hepes (pH 8.2), 150 mM NaCl, 5% glycerol, 0.5 mM TCEP, 1 mM EDTA, 0.1 mM PMSF, 2 mM benzamidine, 5 units/ml benzonase (Novagen), Complete™ EDTA-free protease inhibitors (Roche), 50mM NaF, 20mM β-glycerophosphate and 0.1 μM okadaic acid. After complete mixing the cells were co-lysed by sonication and the lysate was centrifuged for 60 min at 20,000 rpm. The soluble fraction was loaded onto a Strep-Tactin Superflow Cartridge (Qiagen) for purification using the $StrepII^{x2}$ tag on Apc4 as described previously 21. The eluate was then applied to an anti-FLAG M2 Affinity Gel (A220, Sigma) column (directed against the N-terminal FLAG tag on BubR1) and incubated overnight. The APC/C^{MCC} complex was eluted with a 3XFLAG peptide at a concentration of 50 μg/mL. The resulting elution was concentrated to around 1.4 mg/mL and run on a Superose™ 6 3.2/300 (GE Healthcare Life Sciences) gel filtration column pre-equilibrated with gel filtration buffer containing 20 mM Hepes (pH 8.0), 150 mM NaCl and 0.5 mM TCEP. The gel filtration was run on a ÄKTAmicro (GE Healthcare Life Sciences) with a flow rate of 50 μL/min.

An SDS-PAGE of purified APC/C^{MCC} showed both versions of Cdc20, consistent with the incorporation of two distinct subunits of Cdc20 into APC/C^{MCC} (refs 2,20) (Extended Data Fig. 1j). Reconstituted APC/C^{MCC} is stable and homogeneous as shown by size-exclusion chromatography (Extended Data Fig. 2a).

The APC/$C^{Apc15\Delta NTH}$ complex was reconstituted by incubating recombinant APC/$C^{\Delta Apc15}$ with $Apc15^{\Delta NTH}$, at concentrations of 200 nM and 1 μM, respectively, followed by size exclusion chromatography. Anti-Apc15 antibodies were from Santa Cruz Biotechnology (sc-398448).

APC/C ubiquitination assay

To examine APC/C activity towards securin the ubiquitination assay was performed with 60 nM of recombinant human APC/C, 150 nM UBA1, 300 nM UbcH10, 300 nM Ube2S, 20 μM ubiquitin, 2 μM securin, 5 mM ATP, 0.25 mg/mL BSA and 7 nM of recombinant human Cdc20. The ubiquitination products of securin were detected by western blot with either an anti-His antibody (631212; Clontech) or an anti-securin antibody (700791; Invitrogen).

To test the activity of a pre-assembled APC/C^{MCC} complex towards $Cdc20^{MCC}$ (Fig. 5c), ubiquitination reactions were performed with 250 nM of recombinant human APC/$C^{Cdc20\text{-}MCC}$ and 10 μM of UbcH10 (40x excess). To test the activity of APC/C towards the $Cdc20^{MCC}$ from individually purified wild type and mutant $MCC^{BubR1\text{-}StrepII}$ (purification by $StrepII^{x2}$ affinity and gel filtration columns) ubiquitination reactions were performed with 200 nM of recombinant human APC/C^{OA}, 200 nM of recombinant human Cdc20 and either 300 or 600 nM of recombinant human $MCC^{BubR1\text{-}StrepII}$ (Fig. 5d, e). Either with a pre-assembled APC/C^{MCC} complex or with a molar excess of MCC complex over free Cdc20 and APC/C only $Cdc20^{MCC}$ ubiquitination is promoted (data not shown)20. Cdc20 and the ubiquitination products of $Cdc20^{MCC}$ were detected by western blot with an anti-Cdc20 antibody (Cdc20 H-175 sc-8358; Santa Cruz Biotechnology, Inc.).

Electron microscopy

Freshly purified APC/C^{MCC} samples were analysed by negative stain EM to check the sample quality and to obtain a low-resolution reconstruction. Micrographs were collected on a 2k*2k CCD camera fitted to a FEI Spirit electron microscope at an accelerating voltage of 120 kV, operated at a nominal magnification of 42,000 with a resulting pixel size of 2.46 Å/pixel at specimen level. Defocuses were set at approximately -2 μm. Particles were automatically selected using the autoboxer program implemented in EMAN 59. About 150 micrographs per sample were collected yielding ~10,000 particles. After 3D classification performed with RELION 60 only the prominent best class (30-40% of total amount of particles) was used for auto-refinement and final low-resolution structure determination.

Grid preparation for both negative stain and cryo-EM was performed as described previously 32,51. Cryo-EM micrographs were collected with an FEI Tecnai Polara electron microscope at an acceleration voltage of 300 kV and Falcon III direct detector. Micrographs were taken using EPU software (FEI) at a nominal magnification of 78,000, yielding a pixel size of 1.36 Å/pixel at specimen level. A total exposure time of 1.6 s were used at a dose rate of 27 electrons/pixel. Defocus range was set at -2.0 to -4.0 μm. Movie frames were recorded as described 32.

Image processing

Image processing was performed with RELION 1.4 (ref. 60). The initial steps including motion correction, CTF estimation, particle picking and particles sorting by Z-score and 2D classification were performed as described 32. Selected particles were used for a first round of 3D classification with global search and a sampling angular interval of 7.5°, using a 60 Å low-pass filtered $APC^{Cdh1\text{-}Emi1}$ EM map as a reference (ref. 32). Poorly characterized 3D classes, with poorly recognizable features, were discarded at this stage and the remaining particles were refined and corrected for beam-induced particle motion using particle polishing in RELION 61. Polished particles were used for another round of 3D classification with a local search within 15° and a smaller angular sampling interval of 3.7° (Extended Data Figs 4 and 7). The reconstruction generated from all the polished particles, low-pass filtered at 40 Å, was used as reference.

To isolate particles for the $APC/C^{MCC\text{-}Closed}$ state, classes showing closed-like features for the $MCC\text{-}Cdc20^{APC/C}$ module (e.g. proximity to Apc2, Apc4 and Apc10, Extended Data Fig. 4, classes 1-3) were combined and refined. The resultant map was used as reference for a subsequent 3D classification performed with a soft edge mask on the $MCC\text{-}Cdc20^{APC/C}$ module (Extended Data Fig. 4). The mask was created from a map converted from the fitted coordinates of the MCC-Cdc20 module, with three pixel extension and five pixels soft edge width. The MCC-Cdc20 module coordinates were created by fitting the MCC core coordinates and isolated Cdc20 (PDB ID: 4AEZ) 18, on the best $MCC\text{-}Cdc20^{APC/C}$ module density map (Extended Data Fig. 4, class 1).

To isolate particles for the $APC/C^{MCC\text{-}Open}$ state, classes showing open-like features for the MCC-Cdc20 module (e.g. proximity to TPR lobe and loss of contact with Apc2, Apc4 and Apc10, Extended Data Fig. 4, classes 4-5) were refined together. The obtained averaged class was used as a reference for a subsequent 3D classification performed with a larger mask (6 pixel extension and 6 pixel soft edge) created with the $MCC\text{-}Cdc20^{APC/C}$ module coordinates fitted into the corresponding density in the $APC/C^{UbcH10\text{-}MCC}$ reconstruction described below (Extended Data Figs 4 and 7).

To obtain the $APC/C^{\Delta Apc15\text{-}MCC}$ structure the best classes from the 3D classification with local searches step were refined together (Extended Data Fig. 7a, classes 1-3).

To isolate the particles for the $APC/C^{UbcH10\text{-}MCC}$ reconstruction, instead of performing the 3D classification with local search steps, an initial classification with a large mask (similar to $APC/C^{MCC\text{-}Open}$) was performed. The latter allowed the identification of a class that features both the MCC-Cdc20 module and the UbcH10-Apc11-$Apc2^{WHB}$-$Apc2^{\alpha/\beta\ domain}$ assembly 32. A large mask including the latter regions was created by fitting the $MCC\text{-}Cdc20^{APC/C}$ module coordinates and the UbcH10-Apc11-$Apc2^{WHB}$-$Apc2^{\alpha/\beta\ domain}$ assembly (PDB ID: 5A31) 32 in the preliminary $APC/C^{UbcH10\text{-}MCC}$ reconstruction. The latter mask was used for a re-classification of the initial particles and allowed the isolation of the final $APC/C^{UbcH10\text{-}MCC}$ particles (Extended Data Fig. 7c).

All resolution estimates were based on the gold standard Fourier Shell Correlation (FSC) = 0.143 criterion 62. Final FSC curves were calculated using a soft mask (five pixel extension

and three pixel soft edge) of the two independent reconstructions. To visualize high-resolution details, all density maps were corrected for the modulation transfer-function of the detector and sharpened by applying negative B-factors, estimated using automated procedures.

Local resolution maps for all the cryo-EM reconstructions were calculated with RESMAP 63 using a resolution range between 3.5 and 15 Å and displayed with Chimera 64. For comparing structural features among the cryo-EM reconstructions, shown in Fig. 4 and Extended Data Fig. 3, which have different overall resolutions, a common filter of 8.5 Å was applied. This was selected based on the local resolution of the APC/$C^{UbcH10\text{-}MCC}$ map in the region assigned to Apc15 (the main region of relative comparison). APC/$C^{UbcH10\text{-}MCC}$ is the APC/C reconstruction with the lowest overall resolution. Filtering all the reconstruction to 8.5 Å resolution allowed a clear definition of the structural details of both Apc15 and other regions without the appearance of noise. To visualize the connecting density between UbcH10 and Cdc20 the APC/$C^{UbcH10\text{-}MCC}$ map was filtered to 12 Å resolution based on the local resolution of this area and the threshold was slightly lowered.

Model building

Initial fitting and superposition of coordinates was performed with Chimera 64. Model building of APC/C^{MCC} was performed in COOT 65. APC/C platform, TPR lobe, Apc10 and accessory subunit coordinates from the atomic structure of APC/$C^{Cdh1\text{-}Emi1}$ (PDB: 4UI9) 32 were individually rigid body fit into the APC/$C^{MCC\text{-}Closed}$ cryo-EM density. A few regions such as $Apc4^{HBD}$, $Apc5^{NTD}$ and Apc11 were also modified by flexible fitting. The $Apc2^{WHB}$ domain (PDB ID:4YII) 44 was rigid body fit into the corresponding density. $Cdc20^{APC/C}$ IR tail and NTD were rigid body fit from the coordinates of APC/$C^{Cdc20\text{-}Hsl1}$ cryo-EM structure 22. The $Cdc20^{MCC}$ IR tail was modelled by superposing the TPR domain of Apc3 including $Cdc20^{IR}$ from APC/$C^{Cdc20\text{-}Hsl1}$ to the TPR domain of APC/C^{MCC} Apc8A. Two copies of human the $Cdc20^{WD40}$ domain (PDB ID: 4GGA) 66, human C-Mad2 (PDB ID: 2V64) 8 and the human $BubR1^{TPR}$ domain (PDB ID: 3SI5) 67 were rigid body fit on the MCC-Cdc20 module density. $Cdc20^{MCC}$ CRY box, included in the human $Cdc20^{WD40}$ domain crystal structure (PDB ID: 4GGA) 66 was modelled by flexible fitting. In addition, the Cdc20 KILR motif was modelled by rigid body fit of the MCC core crystal structure (PDB ID: 4AEZ) 18 into the corresponding density. A similar procedure was applied to model the first KEN1 and helix-loop-helix region of BubR1. BubR1 D1 and D2 were modelled by rigid body fit of Acm1 D box 3 (PDB ID: 3BH6) 38. Similarly BubR1 A1 and K2 were modelled by flexible fitting of the Acm1 region spanning the A-motif and KEN box as explained in the main text. BubR1 A2 was modelled as a rigid body fit of the Acm1 A-motif. Loop extensions were modelled as idealized polyalanine.

Model refinement was performed with REFMAC 5.8 (ref. 68). A REFMAC weight of 0.04 was defined by cross-validation using half reconstructions 69. A resolution limit of 4.0 Å was used. All available crystal structures or NMR structures were used for secondary structure restraints. The refinement statistics are summarized in Extended Data Table 3b.

Europe PMC Funders Author Manuscripts

Map visualization

Figures were generated using Pymol and Chimera 70. Structural conservation figures were generated using ConSurf 71.

Mass Spectroscopy

Purified proteins were prepared for mass spectrometric analysis by in solution enzymatic digestion, without prior reduction and alkylation. Protein samples were digested with trypsin or elastase (Promega), both at an enzyme to protein ratio of 1:20. The resulting peptides were analysed by nano-scale capillary LC-MS/MS using an Ultimate U3000 HPLC (ThermoScientific Dionex) to deliver a flow of approximately 300 nl/min. A C18 Acclaim PepMap100 5 μm, 100 μm x 20 mm nanoViper (ThermoScientific Dionex), trapped the peptides prior to separation on a C18 Acclaim PepMap100 3 μm, 75 μm x 250 mm nanoViper (ThermoScientific Dionex, San Jose, USA). Peptides were eluted with a 90 min gradient of acetonitrile (2% to 50%). The analytical column outlet was directly interfaced via a nano-flow electrospray ionization source, with a hybrid quadrupole orbitrap mass spectrometer (Q-Exactive Plus Orbitrap, ThermoScientific). LC-MS/MS data were then searched against an in house LMB database using the Mascot search engine (Matrix Science) 72, and the peptide identifications validated using the Scaffold program (Proteome Software Inc.) 73. All data were additionally interrogated manually.

Sequence alignment

Sequence alignment was performed using Jalview 74.

Europe PMC Funders Author Manuscripts

Extended Data

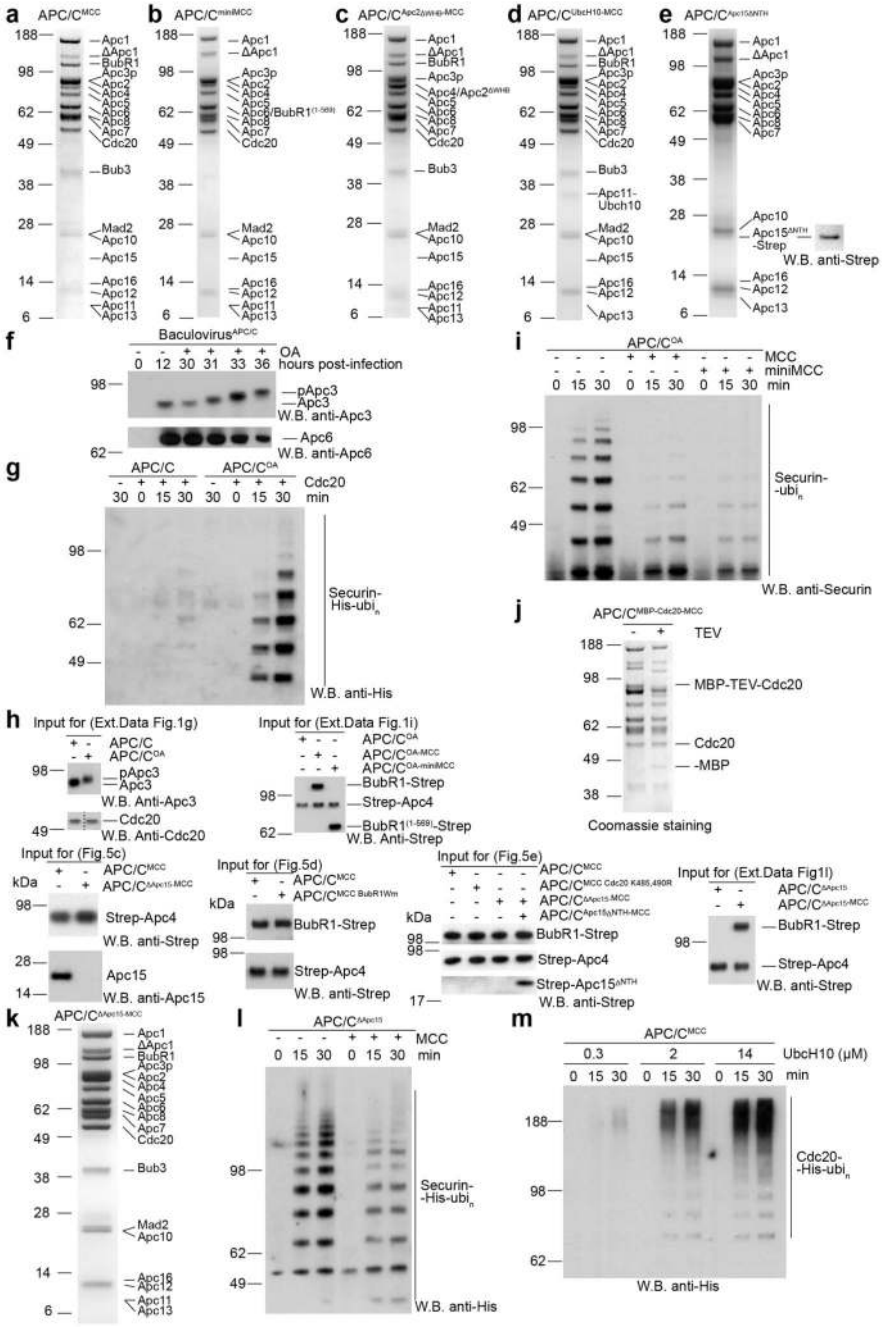

Extended Data Figure 1. Biochemical characterization of recombinant APC/C^{MCC} complex and preparations of wild type and mutant complexes.

a,b,c,d,e SDS PAGE gels (stained with coomassie) of gel filtration peak fraction from wild type and mutant APC/C^{MCC} complexes preparations used in this study. Western blot against Strep tag in (e) confirms the presence of Apc15$^{\Delta NTH\text{-}Strep}$.construct. **f**, Top: Western blot performed with anti-Apc3 antibody to monitor the time-dependent phosphorylation of this subunit induced by okadaic acid (OA) treatment in the APC/C-expressing insect cells.

Bottom: Western blot against was used as a loading control and reflects the decrease in cell viability after addition of OA (data not shown). **g**, Western blot against His_6-tagged ubiquitin of *in vitro* securin ubiquitination assays performed with either APC/C or APC/C^{OA} in either the presence or absence of Cdc20. **h**, the input sample for the ubiquitination assays performed in this study is shown. **i**, Western blot against securin of *in vitro* securin ubiquitination assays performed with APC/C^{OA} and Cdc20 with or without either MCC or miniMCC. **j**, SDS PAGE of APC/C^{MCC} reconstituted with MBP-TEV-$Cdc20^{APC/C}$ and untagged $Cdc20^{MCC}$. MBP-TEV-$Cdc20^{APC/C}$ TEV cleavage products are indicated. **k**, SDS PAGE gels of reconstituted $APC/C^{\Delta Apc15\text{-}MCC}$ complex. **l**, Western blot against His_6-tagged ubiquitin of *in vitro* securin ubiquitination assays performed with APC/C $^{\Delta Apc15}$ and Cdc20 with or without MCC. **m**, Western blot against His_6-tagged ubiquitin of *in vitro* Cdc20 ubiquitination assays performed with APC/C^{MCC} and increasing concentrations of UbcH10. Experiments **g**, **l**, **m** were replicated three times and **i** four times. See Supplementary Fig. 1 for gel source data.

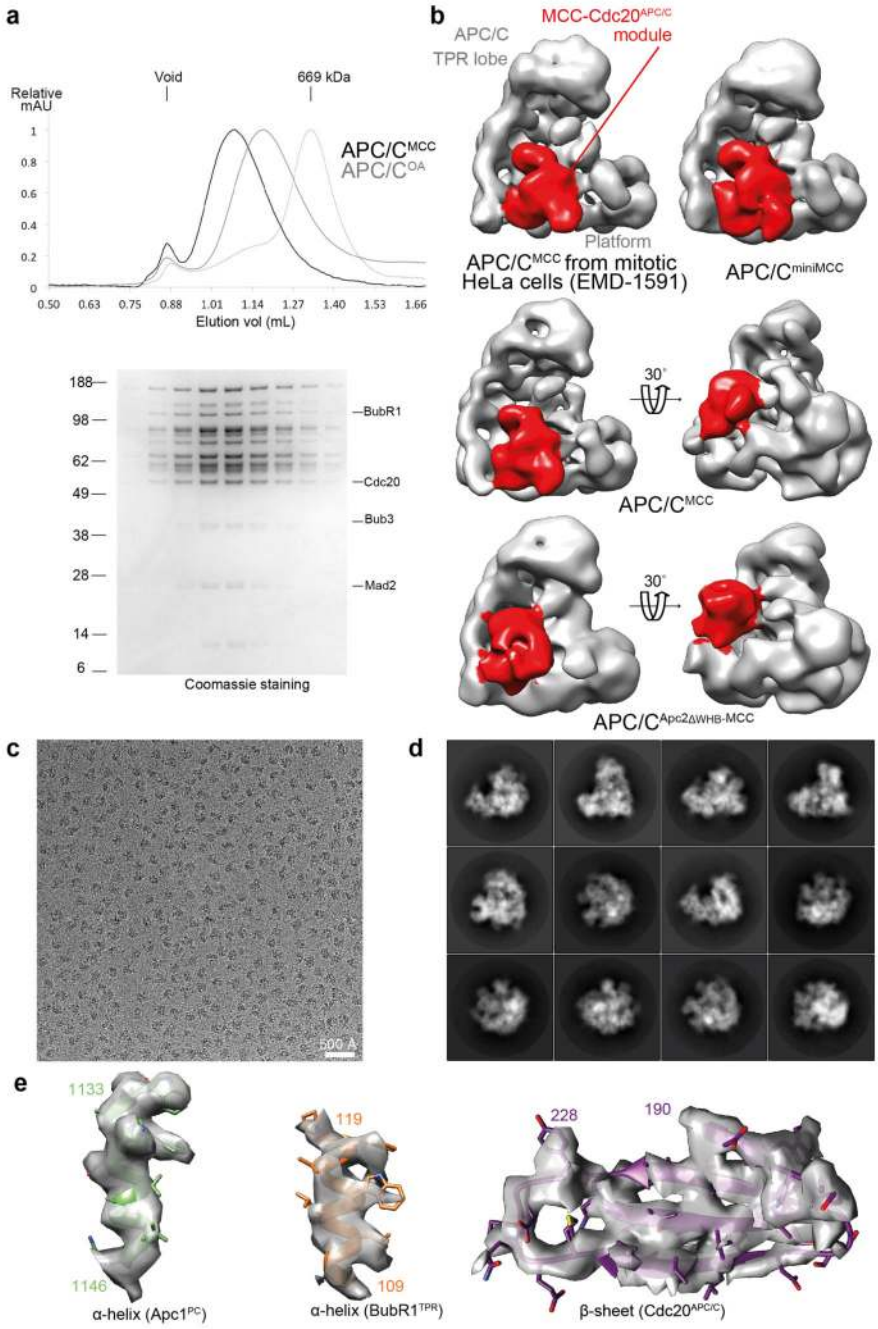

Extended Data Figure 2. Stability of APC/C^{MCC} complex, negative staining-EM reconstructions of APC/C^{MCC} wild type and mutant complexes and Cryo-EM analysis.

a, Top: chromatogram showing the elution profile of the APC/C^{MCC} complex run on a Superose 6 column. Apo APC/C^{OA} and thyroglobulin standard molecular weight marker (669 kDa) are indicated. Bottom: SDS PAGE of the eluted fractions. APC/C^{MCC} elutes earlier than APC/C^{OA}. **b**, Negative stain-EM reconstructions performed for this study and EMD-1591 (ref. 31) are shown. APC/C (grey) and MCC-Cdc20$^{APC/C}$ module (red) are highlighted. The APC/C^{MCC} and APC/C$^{Apc2\Delta WHB\text{-}MCC}$ reconstructions are also shown in

the same orientation as in Figure 4 to facilitate comparisons. **c**, A typical cryo-EM micrograph of APC/C$^{MCC\text{-}Closed}$ representative of 20,234 micrographs. **d**, Gallery of two-dimensional class averages of APC/C$^{MCC\text{-}Closed}$ showing different views representative of 50 two-dimensional classes. **e**, density quality for secondary structures. The APC/C$^{MCC\text{-}Closed}$ map was filtered to 4.0 Å.

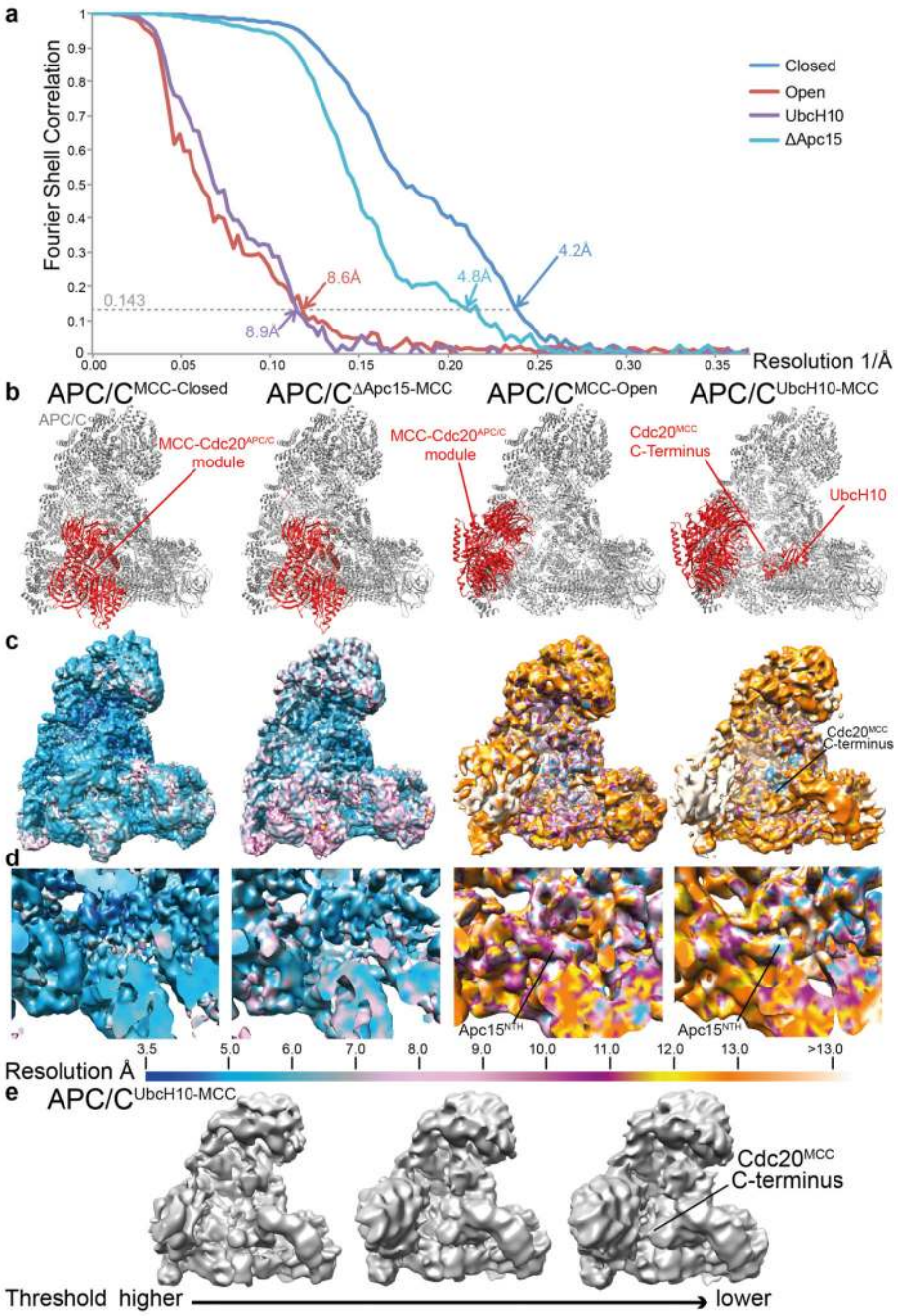

Extended Data Figure 3. Resolution and other Cryo-EM features of APC/C^{MCC} complexes.

Europe PMC Funders Author Manuscripts

a, Fourier Shell Correlation (FSC) curves, (**b, c, d**) local resolution maps calculated with RESMAP 63 are shown for all the cryo-EM reconstructions determined in this study, **b**, ribbon representations of structures shown, **c**, overall views of local resolution maps, **d**, close up of platform region (Apc4, Apc5, Apc15). All the maps shown in (**c**) and (**d**) are filtered to 8.5 Å. Local resolution colour scheme is indicated in the bar at the bottom of (**d**). **e**, the APC/C$^{UbcH10\text{-}MCC}$ reconstruction filtered at 12 Å and shown at different threshold levels. The lowest threshold is the same as in Fig. 5b.

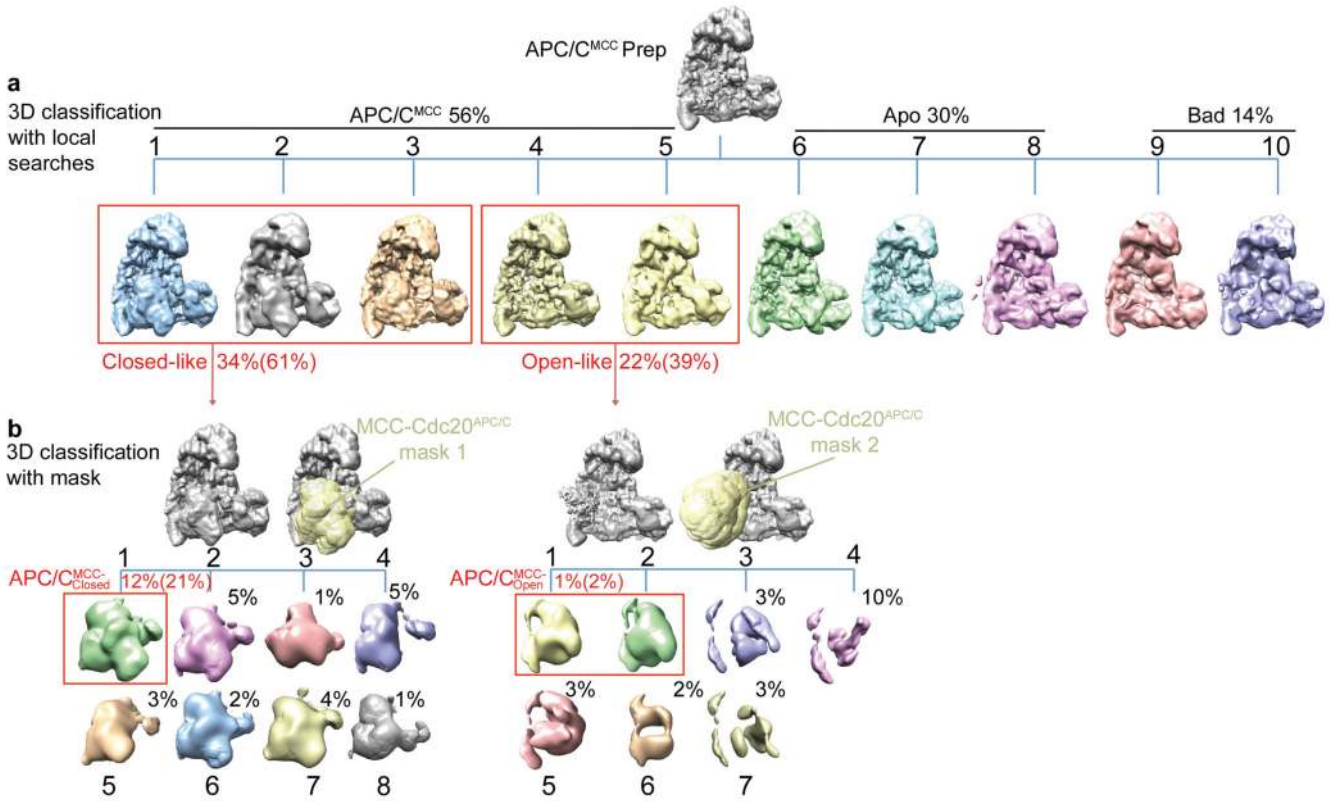

Extended Data Figure 4. Three-dimensional classification of APC/C^{MCC}.

a, b, 3D class averages obtained by classification with local searches (see Methods) are shown in (**a**). Classes 1-5 (56%) show density for the MCC-Cdc20$^{APC/C}$ module with classes 1-3 and 4-5 having a closed-like and an open-like conformation respectively (framed in red, see Methods). Particles from classes 1-3 and 4-5 were separately refined and re-classified using a mask (yellow, see Methods) shown in (**b**) to isolate the best quality particles for APC/C$^{MCC\text{-}Closed}$ (mask 1: left) and APC/C$^{MCC\text{-}Open}$ (mask 2: right). Percentages for each of the classes relative to the total number of selected particles are indicated. The percentages relative to the total number of APC/C^{MCC} particles are indicated in parenthesis.

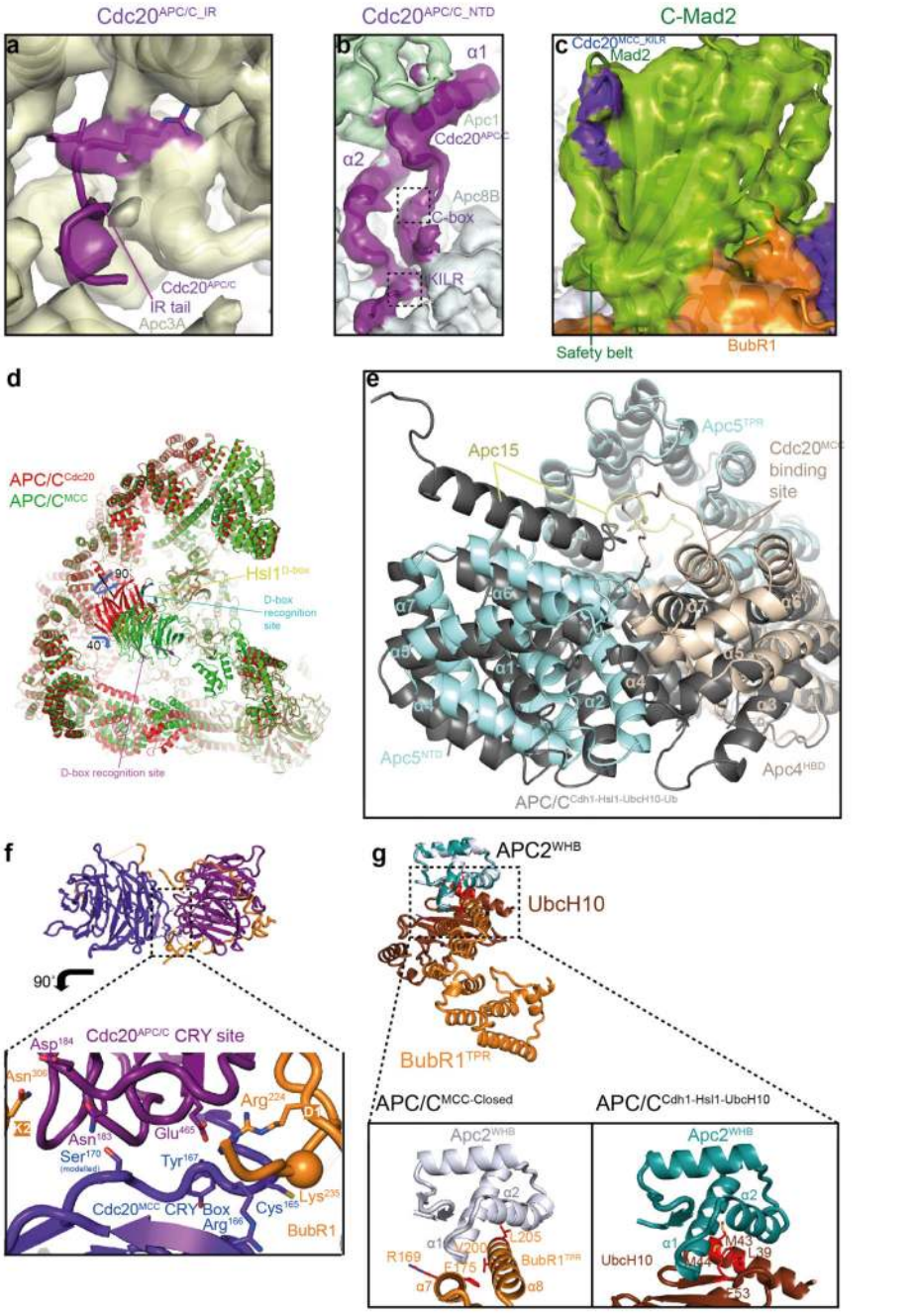

Extended Data Figure 5. Features of the APC/C^{MCC} structure.

a,b,c, Cryo-EM density and fitted coordinates for Cdc20$^{APC/C_IR}$ (**a**), Cdc20$^{APC/C_NTD}$ (**b**), C-Mad2 (**c**) are shown. Colours for each subunit are as for Fig. 1. **d**, Overall superposition of the APC/C$^{Cdc20\text{-}Hsl1}$ structure (red) with the APC/C$^{MCC\text{-}closed}$ structure (green). The Cdc20^{WD40} change of position is illustrated and the blades forming the D-box (yellow) binding pocket is highlighted. **e**, Superposition of Apc4, Apc5 and Apc15 between APC/C$^{Cdh1\text{-}Hsl1\text{-}UbcH10\text{-}Ub}$ structure (grey) and APC/C^{MCC} (subunit colours as in Fig. 1) shows the dramatic conformational change of Apc4^{HBD}, Apc5^{NTD} and Apc15^{NTH} induced by

Europe PMC Funders Author Manuscripts

Europe PMC Funders Author Manuscripts

Cdc20^{MCC} binding to its indicated binding site on Apc4^{HBD}. **f**, close up view of the Cdc20^{MCC} CRY box recognition site of Cdc20$^{APC/C}$. The CRY box also contacts BubR1 in proximity to D1. Colours for each subunit are as for Fig. 1. g, Superposition of the Apc2^{WHB} domains from APC/C^{MCC} and APC/C$^{Cdh1\text{-}Hsl1\text{-}UbcH10\text{-}Ub}$ structures and the corresponding interacting regions of BubR1^{TPR} and UbcH10 are shown. Bottom left: the residues mutated in BubR1^{Wm} that contact Apc2^{WHB} and used in the ubiquitination assay shown in Fig. 5d are indicated (red). Bottom right: Residues of UbcH10 (red) that contact the corresponding site on Apc2^{WHB} ablate APC/C UbcH10-dependent ubiquitination activity 44.

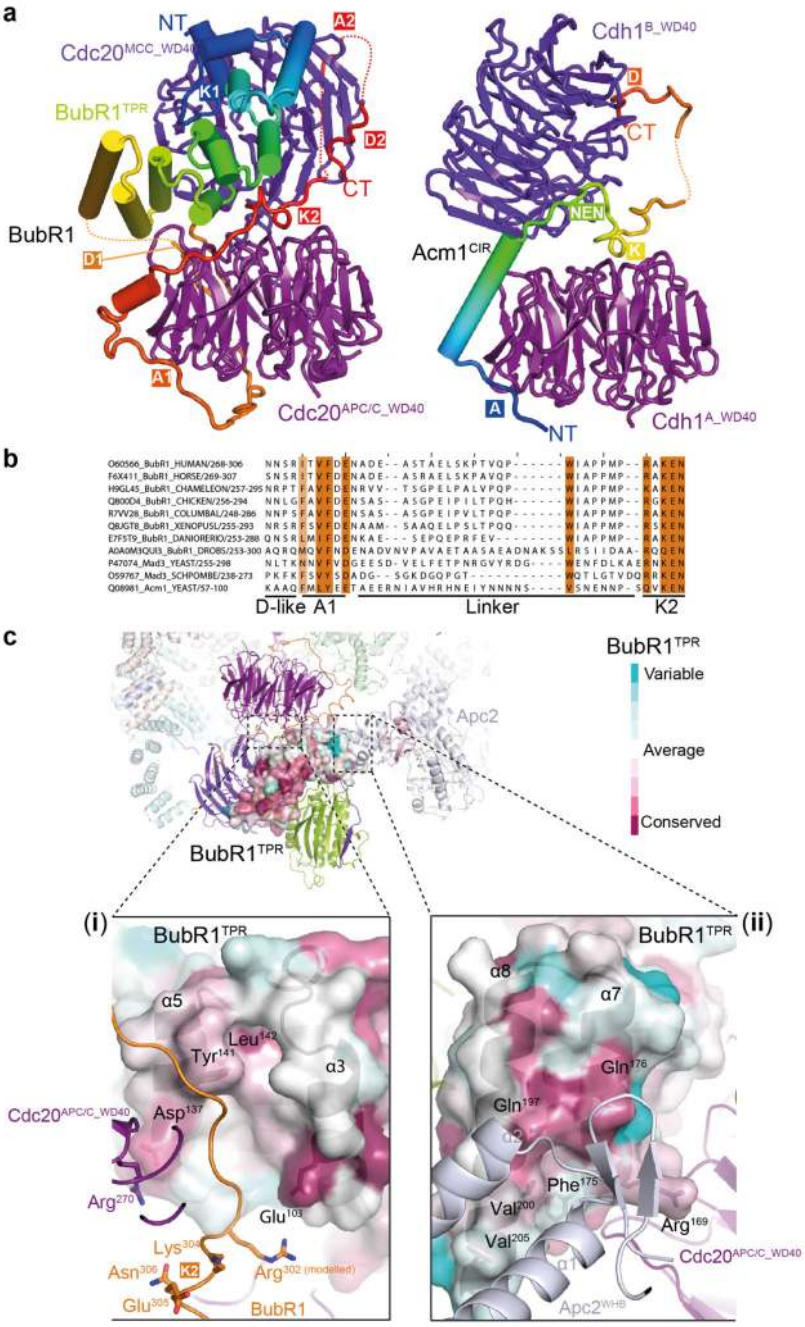

Extended Data Figure 6. Conservation analysis on BubR1$^{A1\text{-}K2}$ and BubR1^{TPR} regions.

a, Similarities in modes of binding of BubR1 to two Cdc20 subunits of APC/C^{MCC} (left) and Acm1 to two Cdh1 subunits in the Acm1-Cdh1 heterotrimer 38 (right). D box, KEN box, NEN box and ABBA motif are labelled as D, K, NEN and A. BubR1 (colour-ramped from blue to red indicating N to C-terminus) mediates Cdc20 dimer interface, whereas Acm1 mediates a Cdh1 dimer interface. **b**, Local sequence alignment performed with BubR1$^{A1\text{-}K2}$ region sequences from several species (described on the left as: sequence identifier_protein name_species/residue number) and the *S. cerevisiae* Acm1$^{A\text{-}KEN}$ region. A D-box-like

feature (corresponding to Emi1$^{D\text{-}box}$ 7-10 positions) 32 precedes the first ABBA motif (A1). A 21-33 residues long linker connects the A1 to the second KEN-box (K2). Conserved positions are highlighted in orange. **c**, ConSurf analysis of the BubR1^{TPR} region highlighting conserved residues on the Cdc20$^{APC/C}$ binding pocket (i) and on the Apc2^{WHB} domain pocket (ii). The Cdc20$^{APC/C}$ binding pocket is required for a functional SAC 67. This site interacts with residues of BubR1 immediately N-terminal to KEN-2, thereby reinforcing their contacts with Cdc20$^{APC/C}$. Residues conservation is indicated in a gradient from cyan to purple. BubR1, Cdc20$^{APC/C}$ and Apc2^{WHB} are coloured as in Fig. 1.

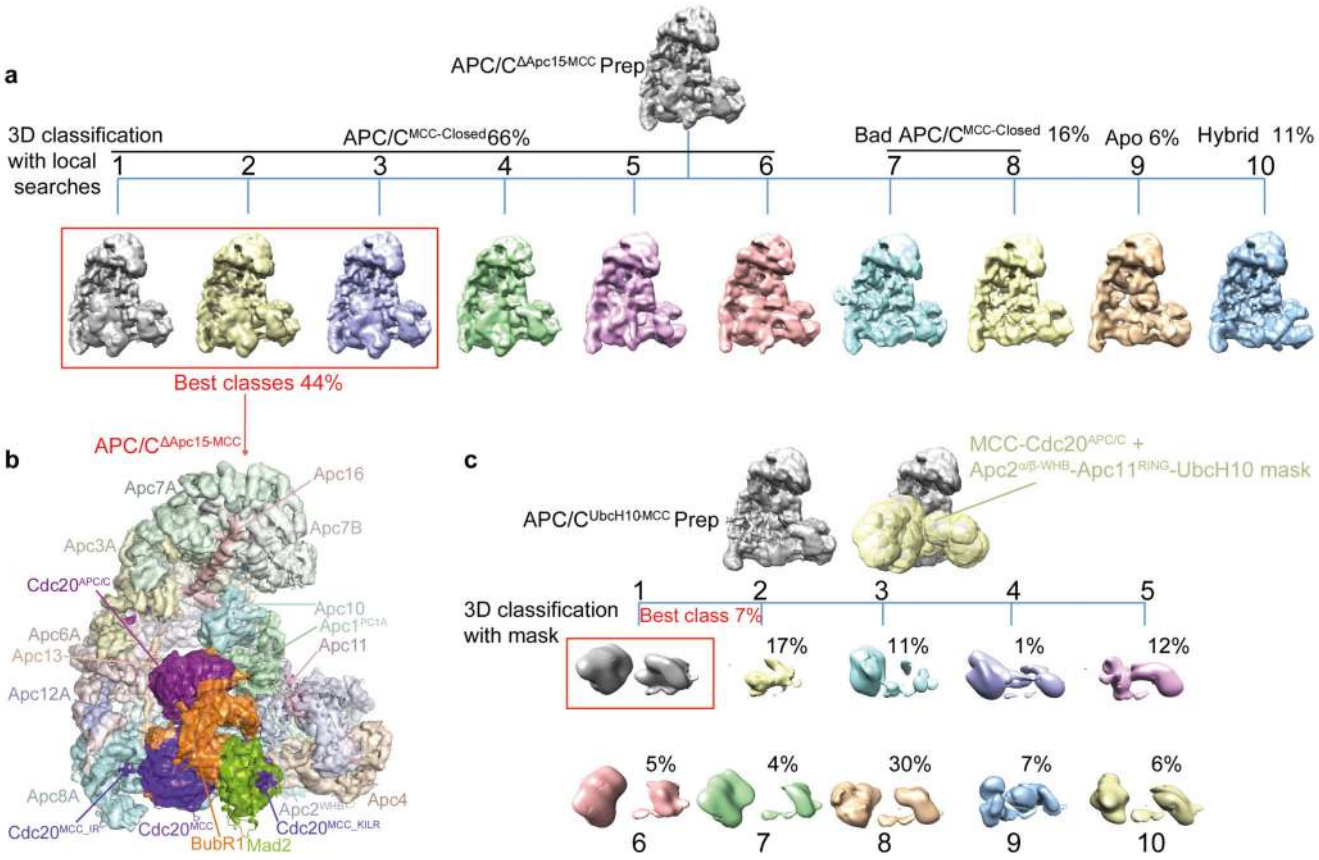

Extended Data Figure 7. Three-dimensional classification of APC/C $^{\Delta Apc15\text{-}MCC}$ and APC/C $^{UbcH10\text{-}MCC}$.

a, 3D class averages obtained by classification with local searches (see Methods) are shown for APC/C$^{\Delta Apc15\text{-}MCC}$. Particles from classes 1-3 were refined together for obtaining the final APC/C$^{\Delta Apc15\text{-}MCC}$ reconstruction shown in (**b**). The APC/C$^{\Delta Apc15\text{-}MCC}$ map was filtered to 4.8 Å. **c**, 3D class averages obtained by classification using a mask (yellow, see Methods) are shown for APC/C $^{UbcH10\text{-}MCC}$. Class 1 was used for the final reconstruction. Percentages relative to the total amount of particles are indicated for each of the classes.

Europe PMC Funders Author Manuscripts

Europe PMC Funders Author Manuscripts

Extended Data Table 1

Summary of phosphorylation sites in APC/C complexes used in this study.

Protein	Phospho-sites	untreated	OA	Reference
Apc1	LWS51DGA			57
	QEVT65IHE			57
	PPGS202PRE			56,57,58
	RVKS276EEE			56
	QGGT291PQN			56,57,58
	NVAT297SSS			56,57,58
	HLRS307LSK			57 (Interphase)
	RSLS309KGD			57
	KGDS313PVT			57
	SPVT316SPF			57
	HSRS341PSI			56,57,58
	RSPS343ISN			56,57,58
	PSIS345NMA			56,57
	AALS351RAH			56,57,58
	RAHS355PAL			56,57,58
	GVHS362FSG			56,57,58
	HSFS364GVQ			56,57
	FNIS372SHN			56,57
	NISS373HNQ			56,57
	HNQS377PKR			56,57,58
	ISHS386PNS			57 (Interphase)
	SNGS394FLA			57
	RPST530PLD			57,58
	DGVS536TPK			56
	GVST537PKP			56,57
	LLGS547LDE			57
	VLLS555PVP			57,58
	LHDS569LYN			57
	SLY571NED			56
	GSLS688PVI			56,57,58
	ARPS699ETG			57
	ETGS703DDD			57
	LCLS731PSE			58
	RHST921SVS			57
	HSTS922VSS			57
	KHKS1347PSY			57

Protein	Phospho-sites	untreated	OA	Reference
	AHVY1463IIA			
Apc2	ELDS205RYA			58
	RPAS314PEA			56,57,58
	GQDS470EDD			57
	RRSS499DII			
	HQFS532FSP			58
	FSFS534PER			56,58
	LIDS732DDE	N.D.		57 (Interphase)
	DDES736DSG	N.D.		57 (Interphase)
	ESDS738GMA	N.D.		57 (Interphase)
Apc3	TVLT203ETP			58
	LTET205PQD			56,57,58
	PQDT209IEL			56
	SKYS225LNT			56,57,58
	AVIS241PDT			56,57
	ETPS291PGD			56
	GDGS296YLQ			56
	LQNY301TNT			56
	QNYT302NTP			56
	YTNT304PPV			56
	SVFS334QSG			58
	SGNS339REV			58
	REVT343PIL			57,58
	QTST358TPQ			58
	TSTT359PQV			58
	QVLS364PTI			56,57
	LSPT366ITS			56,58
	PTIT368SPP			56,58
	TITS369PPN			56,57,58
	LFTS384DSS			58
	SDSS387TTK			57,58
	INDS426LEI			56,57,58
	LEIT430KLD			56
	KLDS434SII			56,57
	LDSS435IIS			56,57,58
	SIIS438EGK			57,58
	STIT446PQI			56,57,58
	SSMT809DAD			
	ADDT814QLH			

Protein	Phospho-sites	untreated	OA	Reference
	AAES821DEF			
Apc4	KGKY469FNV			56
	EVLS777ESE			57,58
	LSES779EAE			56
Apc5	MELT178SRD			57
	ELTS179RDE			57
	LDVS195VRE			56,58
	KALT232PAS			58
Apc6	FEKY107LKD			56,58
	KDES112GFK			56,57
	NIIS559PPW			56,57,58
	TGLT580PLE			56,57,58
	LETS585RKT			57,58
	SRPS595LEE			56
Apc7	VRPS119TGN			56
	TGNS123AST			56,57
	NSAS125TPQ			56,57
	SAST126PQS			57,58
	DQKS545LEG			
	KEES557PTD			
Apc8	VAVT13AAV			
	QGET556PTT			56,57,58
	TPTT559EVP			56,58
	ETPT564TEV			56,57,58
	NTPT584RRV			56,57
	RRVS588PLN			56,57,58
	LNLS593SVT			57
	NLSS594VTP			57
	SSVT596P			57,58

The red shadowing shows the presence of phosphorylation sites and white indicates its absence

Extended Data Table 2

Glossary of terms and abbreviations used in this study.

Abbreviation	Full name
APC/C	Anaphase-promoting complex/cyclosome (Apc1-Apc8, Apc10-Apc13, Apc15, Apc16)
MCC	Mitotic checkpoint complex (Cdc20, Mad2, BubR1, Bub3)
SAC	Spindle assembly checkpoint
Cdc20	Mitotic APC/C coactivator subunit
Cdh1	Late mitotic APC/C coactivator subunit

Abbreviation	Full name
UbcH10	Initiating E2
Ube2S	Elongating E2
APC/C^{Cdc20}	APC/C – Cdc20 complex
APC/C^{Cdh1}	APC/C – Cdh1 complex
APC/C^{MCC}	Inhibited APC/C^{Cdc20} – MCC complex
APC/$C^{MCC\text{-}Closed}$	Closed conformation of APC/C^{MCC}
APC/$C^{MCC\text{-}Open}$	Open conformation of APC/C^{MCC}
APC/$C^{UbcH10\text{-}MCC}$	APC/C^{MCC} – UbcH10 complex
APC/$C^{Cdh1\text{-}Emi1}$	APC/C^{Cdh1} – Emi1 complex
APC/$C^{Cdh1,substrate,UbcH10\text{-}Ub}$	APC/C^{Cdh1} – substrate-UbcH10 complex
APC/$C^{\Delta Apc15}$	APC/C with Apc15 deleted
APC/C^{OA}	Reconstituted phosphorylated APC/C isolated from BV/insect cells cultures incubated with okadaic acid
$Cdc20^{APC/C}$	Cdc20 subunit of APC/C^{Cdc20}
$Cdc20^{MCC}$	Cdc20 subunit of MCC
$Cdc20^{APC/C\text{-}WD40}$	WD40 domain of Cdc20 subunit of APC/C^{Cdc20}
C-Mad2	Closed conformation of Mad2
C-$Mad2^{SB}$	C-mad2 safety belt
O-Mad2	Open conformation of Mad2
IR tail	Apc3 and Apc8 interacting C-terminal Ile-Arg motif of Cdc20 (Cdh1 and Apc10)
C box	Apc8 interacting motif of Cdc20 and Cdh1 (DRYIPxR)
KILR motif	C-Mad2-interaction motif of $Cdc20^{MCC}$ and an Apc8-interacting motif of $Cdc20^{APC/C}$
LR tail	Leu-Arg-Arg-Leu C-terminal motif common to Ube2S and Emi1
D box	APC/C degron: RxxLxx[IV]xN
KEN box	APC/C degron: KEN
ABBA motif (A motif)	APC/C degron: Fx[ILV][FHY]x[DE]
CRY motif	APC/C degron: CRY
D1, D2	D-1 box of BubR1, D-2 box of BubR1
A1, A2	ABBA-1 motif of BubR1, ABBA-2 motif of BubR1
K1, K2	KEN-1 box of BubR1, KEN-2 box of BubR1
$Apc4^{HBD}$	Helix bundle domain of Apc4
$Apc5^{NTD}$	N-terminal domain domain of Apc5
$Apc15^{NTH}$	N-terminal helix of Apc15
$BubR1^{TPR}$	BubR1 tetratricopeptide (TPR) domain

Extended Data Table 3
Summary of cryo-EM data and statistics.

a. Statistics of all cryo-EM reconstructions

Samples	Micrographs collected	Particles used for final reconstruction	Resolution (Å)
APC/C$^{MCC\text{-}Closed}$	20,234	155,263	4.2
APC/C$^{MCC\text{-}Open}$		6,188	8.6
APC/C$^{UbcH10\text{-}MCC}$	2,340	8,491	8.9
APC/C$^{\Delta Apc15\text{-}MCC}$	5,054	163,308	4.8

b. Statistics of all cryo-EM structure determination

Data collection				
EM	FEI Polara, 300K eV			
Detector	FEI Falcon III			
Pixel size (Å)	1.36			
Defocus range (μm)	2.0-4.0			
Reconstruction	APC/C$^{MCC\text{-}Closed}$	APC/C$^{MCC\text{-}Open}$	APC/C$^{UbcH10\text{-}MCC}$	APC/C$^{\Delta Apc15\text{-}MCC}$
Software	RELION 1.4	RELION 1.4	RELION 1.4	RELION 1.4
Accuracy of rotation (degrees)	1.318	2.594	3.235	1.61
Accuracy of translations (pixels)	0.843	1.763	2.09	1.08
Final resolution (Å)	4.2	8.6	8.9	4.8
Refinement	APC/C$^{MCC\text{-}Closed}$			
Software	RefMac 5.8			
Refmac weight	0.04			
Resolution limit (Å)	4.0			
Residue number	9,014			
Average Fourier shell correlation	0.761			
R factor	0.2505			
Rms bind length (Å)	0.0126			
Rms bond angle (°)	1.746			
Validation				
Ramachandran plot				
Preferred	8427 (93.49%)			
Allowed	353 (3.92%)			
Outliers	234 (2.60%)			

Supplementary Material

Refer to Web version on PubMed Central for supplementary material.

Acknowledgments

This work was supported by a Cancer Research UK grant (C576/A14109) and the Medical Research Council (MRC_UP_1201/6) to DB and a Long Term EMBO Fellowship to C.A. We thank members of the Barford group for discussions, X. Bai and S. Scheres for their help with RELION; C. Savva and S. Chen for EM facilities; J. Grimmett and T. Darling for computing and W. Zachariae and J. Pines for their invaluable advice and JP for communicating data prior to publication.

References

1. Meyer HJ, Rape M. Processive ubiquitin chain formation by the anaphase-promoting complex. Seminars in cell & developmental biology. 2011; 22:544–550. [PubMed: 21477659]
2. Primorac I, Musacchio A. Panta rhei: the APC/C at steady state. The Journal of cell biology. 2013; 201:177–189. [PubMed: 23589490]
3. Lara-Gonzalez P, Westhorpe FG, Taylor SS. The spindle assembly checkpoint. Current biology: CB. 2012; 22:R966–980. [PubMed: 23174302]
4. Musacchio A. The Molecular Biology of Spindle Assembly Checkpoint Signaling Dynamics. Current biology : CB. 2015; 25:R1002–1018. [PubMed: 26485365]
5. Hoyt MA, Totis L, Roberts BTS. cerevisiae genes required for cell cycle arrest in response to loss of microtubule function. Cell. 1991; 66:507–517. [PubMed: 1651171]
6. Li R, Murray AW. Feedback control of mitosis in budding yeast. Cell. 1991; 66:519–531. [PubMed: 1651172]
7. De Antoni A, et al. The Mad1/Mad2 complex as a template for Mad2 activation in the spindle assembly checkpoint. Current biology : CB. 2005; 15:214–225. [PubMed: 15694304]
8. Mapelli M, Massimiliano L, Santaguida S, Musacchio A. The Mad2 conformational dimer: structure and implications for the spindle assembly checkpoint. Cell. 2007; 131:730–743. [PubMed: 18022367]
9. Kulukian A, Han JS, Cleveland DW. Unattached kinetochores catalyze production of an anaphase inhibitor that requires a Mad2 template to prime Cdc20 for BubR1 binding. Developmental cell. 2009; 16:105–117. [PubMed: 19154722]
10. Luo X, Tang Z, Rizo J, Yu H. The Mad2 spindle checkpoint protein undergoes similar major conformational changes upon binding to either Mad1 or Cdc20. Molecular cell. 2002; 9:59–71. [PubMed: 11804586]
11. Sironi L, et al. Crystal structure of the tetrameric Mad1-Mad2 core complex: implications of a 'safety belt' binding mechanism for the spindle checkpoint. The EMBO journal. 2002; 21:2496–2506. [PubMed: 12006501]
12. Sudakin V, Chan GK, Yen TJ. Checkpoint inhibition of the APC/C in HeLa cells is mediated by a complex of BUBR1, BUB3, CDC20, and MAD2. The Journal of cell biology. 2001; 154:925–936. [PubMed: 11535616]
13. Hardwick KG, Johnston RC, Smith DL, Murray AW. MAD3 encodes a novel component of the spindle checkpoint which interacts with Bub3p, Cdc20p, and Mad2p. The Journal of cell biology. 2000; 148:871–882. [PubMed: 10704439]
14. Fang G. Checkpoint protein BubR1 acts synergistically with Mad2 to inhibit anaphase-promoting complex. Molecular biology of the cell. 2002; 13:755–766. [PubMed: 11907259]
15. Davenport J, Harris LD, Goorha R. Spindle checkpoint function requires Mad2-dependent Cdc20 binding to the Mad3 homology domain of BubR1. Exp Cell Res. 2006; 312:1831–1842. [PubMed: 16600213]
16. Burton JL, Solomon MJ. Mad3p, a pseudosubstrate inhibitor of APCCdc20 in the spindle assembly checkpoint. Genes & development. 2007; 21:655–667. [PubMed: 17369399]
17. Nilsson J, Yekezare M, Minshull J, Pines J. The APC/C maintains the spindle assembly checkpoint by targeting Cdc20 for destruction. Nature cell biology. 2008; 10:1411–1420. [PubMed: 18997788]
18. Chao WC, Kulkarni K, Zhang Z, Kong EH, Barford D. Structure of the mitotic checkpoint complex. Nature. 2012; 484:208–213. [PubMed: 22437499]
19. Tang Z, Bharadwaj R, Li B, Yu H. Mad2-Independent inhibition of APCCdc20 by the mitotic checkpoint protein BubR1. Developmental cell. 2001; 1:227–237. [PubMed: 11702782]
20. Izawa D, Pines J. The mitotic checkpoint complex binds a second CDC20 to inhibit active APC/C. Nature. 2015; 517:631–634. [PubMed: 25383541]
21. Chang L, Zhang Z, Yang J, McLaughlin SH, Barford D. Molecular architecture and mechanism of the anaphase-promoting complex. Nature. 2014; 513:388–393. [PubMed: 25043029]

22. Zhang S, et al. Molecular mechanism of APC/C activation by mitotic phosphorylation. Nature. 2016; 533:260–264. [PubMed: 27120157]
23. Reddy SK, Rape M, Margansky WA, Kirschner MW. Ubiquitination by the anaphase-promoting complex drives spindle checkpoint inactivation. Nature. 2007; 446:921–925. [PubMed: 17443186]
24. Stegmeier F, et al. Anaphase initiation is regulated by antagonistic ubiquitination and deubiquitination activities. Nature. 2007; 446:876–881. [PubMed: 17443180]
25. Pan J, Chen RH. Spindle checkpoint regulates Cdc20p stability in Saccharomyces cerevisiae. Genes & development. 2004; 18:1439–1451. [PubMed: 15198982]
26. King EM, van der Sar SJ, Hardwick KG. Mad3 KEN boxes mediate both Cdc20 and Mad3 turnover, and are critical for the spindle checkpoint. PloS one. 2007; 2:e342. [PubMed: 17406666]
27. Ge S, Skaar JR, Pagano M. APC/C- and Mad2-mediated degradation of Cdc20 during spindle checkpoint activation. Cell cycle. 2009; 8:167–171. [PubMed: 19098431]
28. Foster SA, Morgan DO. The APC/C subunit Mnd2/Apc15 promotes Cdc20 autoubiquitination and spindle assembly checkpoint inactivation. Molecular cell. 2012; 47:921–932. [PubMed: 22940250]
29. Uzunova K, et al. APC15 mediates CDC20 autoubiquitylation by APC/C(MCC) and disassembly of the mitotic checkpoint complex. Nature structural & molecular biology. 2012; 19:1116–1123.
30. Mansfeld J, Collin P, Collins MO, Choudhary JS, Pines J. APC15 drives the turnover of MCC-CDC20 to make the spindle assembly checkpoint responsive to kinetochore attachment. Nature cell biology. 2011; 13:1234–1243. [PubMed: 21926987]
31. Herzog F, et al. Structure of the anaphase-promoting complex/cyclosome interacting with a mitotic checkpoint complex. Science. 2009; 323:1477–1481. [PubMed: 19286556]
32. Chang L, Zhang Z, Yang J, McLaughlin SH, Barford D. Atomic structure of the APC/C and its mechanism of protein ubiquitination. Nature. 2015; 522:450–454. [PubMed: 26083744]
33. Malureanu LA, et al. BubR1 N terminus acts as a soluble inhibitor of cyclin B degradation by APC/C(Cdc20) in interphase. Developmental cell. 2009; 16:118–131. [PubMed: 19154723]
34. Suijkerbuijk SJ, et al. The vertebrate mitotic checkpoint protein BUBR1 is an unusual pseudokinase. Developmental cell. 2012; 22:1321–1329. [PubMed: 22698286]
35. Han JS, et al. Catalytic assembly of the mitotic checkpoint inhibitor BubR1-Cdc20 by a Mad2-induced functional switch in Cdc20. Molecular cell. 2013; 51:92–104. [PubMed: 23791783]
36. Lara-Gonzalez P, Scott MI, Diez M, Sen O, Taylor SS. BubR1 blocks substrate recruitment to the APC/C in a KEN-box-dependent manner. Journal of cell science. 2011
37. Izawa D, Pines J. How APC/C-Cdc20 changes its substrate specificity in mitosis. Nature cell biology. 2011; 13:223–233. [PubMed: 21336306]
38. He J, et al. Insights into Degron Recognition by APC/C Coactivators from the Structure of an Acm1-Cdh1 Complex. Molecular cell. 2013; 50:649–660. [PubMed: 23707760]
39. Elowe S, et al. Uncoupling of the spindle-checkpoint and chromosome-congression functions of BubR1. Journal of cell science. 2010; 123:84–94. [PubMed: 20016069]
40. Lischetti T, Zhang G, Sedgwick GG, Bolanos-Garcia VM, Nilsson J. The internal Cdc20 binding site in BubR1 facilitates both spindle assembly checkpoint signalling and silencing. Nature communications. 2014; 5:5563.
41. Di Fiore B, et al. The ABBA motif binds APC/C activators and is shared by APC/C substrates and regulators. Developmental cell. 2015; 32:358–372. [PubMed: 25669885]
42. Diaz-Martinez LA, et al. The Cdc20-binding Phe box of the spindle checkpoint protein BubR1 maintains the mitotic checkpoint complex during mitosis. The Journal of biological chemistry. 2015; 290:2431–2443. [PubMed: 25505175]
43. Kaisari S, Sitry-Shevah D, Miniowitz-Shemtov S, Hershko A. Intermediates in the assembly of mitotic checkpoint complexes and their role in the regulation of the anaphase-promoting complex. Proceedings of the National Academy of Sciences of the United States of America. 2016; 113:966–971. [PubMed: 26755599]
44. Brown NG, et al. RING E3 mechanism for ubiquitin ligation to a disordered substrate visualized for human anaphase-promoting complex. Proceedings of the National Academy of Sciences of the United States of America. 2015; 112:5272–5279. [PubMed: 25825779]

45. Varetti G, Guida C, Santaguida S, Chiroli E, Musacchio A. Homeostatic control of mitotic arrest. Molecular cell. 2011; 44:710–720. [PubMed: 22152475]
46. Garnett MJ, et al. UBE2S elongates ubiquitin chains on APC/C substrates to promote mitotic exit. Nature cell biology. 2009; 11:1363–1369. [PubMed: 19820702]
47. Williamson A, et al. Identification of a physiological E2 module for the human anaphase-promoting complex. Proceedings of the National Academy of Sciences of the United States of America. 2009; 106:18213–18218. [PubMed: 19822757]
48. Kelly A, Wickliffe KE, Song L, Fedrigo I, Rape M. Ubiquitin chain elongation requires e3-dependent tracking of the emerging conjugate. Molecular cell. 2014; 56:232–245. [PubMed: 25306918]
49. Reis A, Levasseur M, Chang HY, Elliott DJ, Jones KT. The CRY box: a second APCcdh1-dependent degron in mammalian cdc20. EMBO reports. 2006; 7:1040–1045. [PubMed: 16878123]
50. Plechanovova A, Jaffray EG, Tatham MH, Naismith JH, Hay RT. Structure of a RING E3 ligase and ubiquitin-loaded E2 primed for catalysis. Nature. 2012; 489:115–120. [PubMed: 22842904]
51. Zhang Z, et al. Recombinant expression, reconstitution and structure of human anaphase-promoting complex (APC/C). The Biochemical journal. 2013; 449:365–371. [PubMed: 23078409]
52. Zhang Z, Yang J, Barford D. Recombinant expression and reconstitution of multiprotein complexes by the USER cloning method in the insect cell-baculovirus expression system. Methods. 2016; 95:13–25. [PubMed: 26454197]
53. van den Ent F, Lowe J. RF cloning: a restriction-free method for inserting target genes into plasmids. Journal of biochemical and biophysical methods. 2006; 67:67–74. [PubMed: 16480772]
54. Yudkovsky Y, Shteinberg M, Listovsky T, Brandeis M, Hershko A. Phosphorylation of Cdc20/fizzy negatively regulates the mammalian cyclosome/APC in the mitotic checkpoint. Biochem Biophys Res Commun. 2000; 271:299–304. [PubMed: 10799291]
55. Labit H, et al. Dephosphorylation of Cdc20 is required for its C-box-dependent activation of the APC/C. The EMBO journal. 2012; 31:3351–3362. [PubMed: 22713866]
56. Kraft C, et al. Mitotic regulation of the human anaphase-promoting complex by phosphorylation. The EMBO journal. 2003; 22:6598–6609. [PubMed: 14657031]
57. Hegemann B, et al. Systematic phosphorylation analysis of human mitotic protein complexes. Science signaling. 2011; 4:rs12. [PubMed: 22067460]
58. Steen JA, et al. Different phosphorylation states of the anaphase promoting complex in response to antimitotic drugs: a quantitative proteomic analysis. Proceedings of the National Academy of Sciences of the United States of America. 2008; 105:6069–6074. [PubMed: 18420821]
59. Ludtke SJ, Baldwin PR, Chiu W. EMAN: semiautomated software for high-resolution single-particle reconstructions. Journal of structural biology. 1999; 128:82–97. [PubMed: 10600563]
60. Scheres SH. RELION: implementation of a Bayesian approach to cryo-EM structure determination. Journal of structural biology. 2012; 180:519–530. [PubMed: 23000701]
61. Bai XC, Fernandez IS, McMullan G, Scheres SH. Ribosome structures to near-atomic resolution from thirty thousand cryo-EM particles. eLife. 2013; 2:e00461. [PubMed: 23427024]
62. Chen S, et al. High-resolution noise substitution to measure overfitting and validate resolution in 3D structure determination by single particle electron cryomicroscopy. Ultramicroscopy. 2013; 135:24–35. [PubMed: 23872039]
63. Kucukelbir A, Sigworth FJ, Tagare HD. Quantifying the local resolution of cryo-EM density maps. Nature methods. 2014; 11:63–65. [PubMed: 24213166]
64. Pettersen EF, et al. UCSF Chimera--a visualization system for exploratory research and analysis. Journal of computational chemistry. 2004; 25:1605–1612. [PubMed: 15264254]
65. Emsley P, Lohkamp B, Scott WG, Cowtan K. Features and development of Coot. Acta crystallographica. Section D, Biological crystallography. 2010; 66:486–501. [PubMed: 20383002]
66. Tian W, et al. Structural analysis of human Cdc20 supports multisite degron recognition by APC/C. Proceedings of the National Academy of Sciences of the United States of America. 2012; 109:18419–18424. [PubMed: 23091007]

67. Bolanos-Garcia VM, et al. Structure of a Blinkin-BUBR1 complex reveals an interaction crucial for kinetochore-mitotic checkpoint regulation via an unanticipated binding Site. Structure. 2011; 19:1691–1700. [PubMed: 22000412]

68. Murshudov GN, et al. REFMAC5 for the refinement of macromolecular crystal structures. Acta Crystallogr D Biol Crystallogr. 2011; 67:355–367. [PubMed: 21460454]

69. Fernandez IS, Bai XC, Murshudov G, Scheres SH, Ramakrishnan V. Initiation of translation by cricket paralysis virus IRES requires its translocation in the ribosome. Cell. 2014; 157:823–831. [PubMed: 24792965]

70. Yang Z, et al. UCSF Chimera, MODELLER, and IMP: an integrated modeling system. Journal of structural biology. 2012; 179:269–278. [PubMed: 21963794]

71. Landau M, et al. ConSurf 2005: the projection of evolutionary conservation scores of residues on protein structures. Nucleic acids research. 2005; 33:W299–302. [PubMed: 15980475]

72. Perkins DN, Pappin DJ, Creasy DM, Cottrell JS. Probability-based protein identification by searching sequence databases using mass spectrometry data. Electrophoresis. 1999; 20:3551–3567. [PubMed: 10612281]

73. Keller A, Nesvizhskii AI, Kolker E, Aebersold R. Empirical statistical model to estimate the accuracy of peptide identifications made by MS/MS and database search. Analytical chemistry. 2002; 74:5383–5392. [PubMed: 12403597]

74. Waterhouse AM, Procter JB, Martin DM, Clamp M, Barton GJ. Jalview Version 2--a multiple sequence alignment editor and analysis workbench. Bioinformatics. 2009; 25:1189–1191. [PubMed: 19151095]

Europe PMC Funders Author Manuscripts

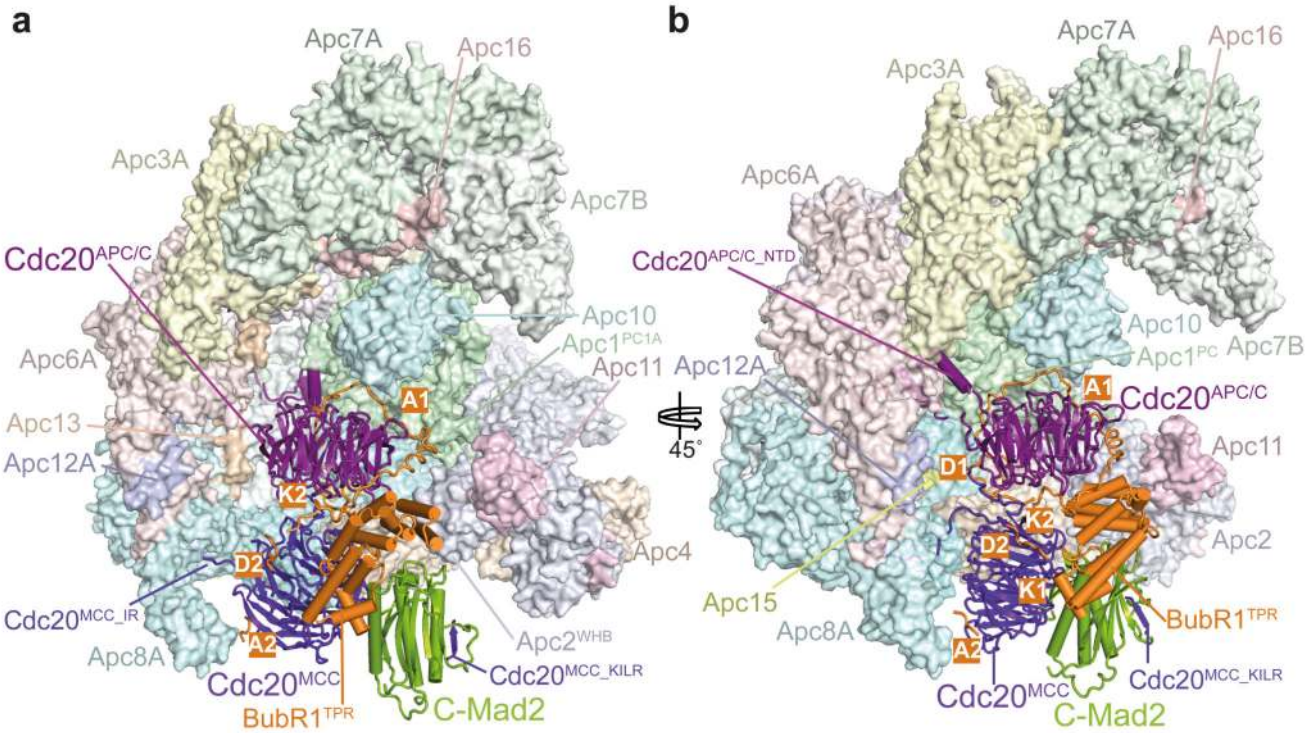

Figure 1. Overall structure of the APC/C^{MCC} complex.

a, b. Two views of APC/C^{MCC}. The MCC-Cdc20$^{APC/C}$ module is shown as a cartoon and the APC/C in a surface representation. BubR1 forms extensive contacts with Cdc20$^{APC/C}$ and Apc2. BubR1 inhibitory degrons visible in these views are highlighted.

Europe PMC Funders Author Manuscripts

Europe PMC Funders Author Manuscripts

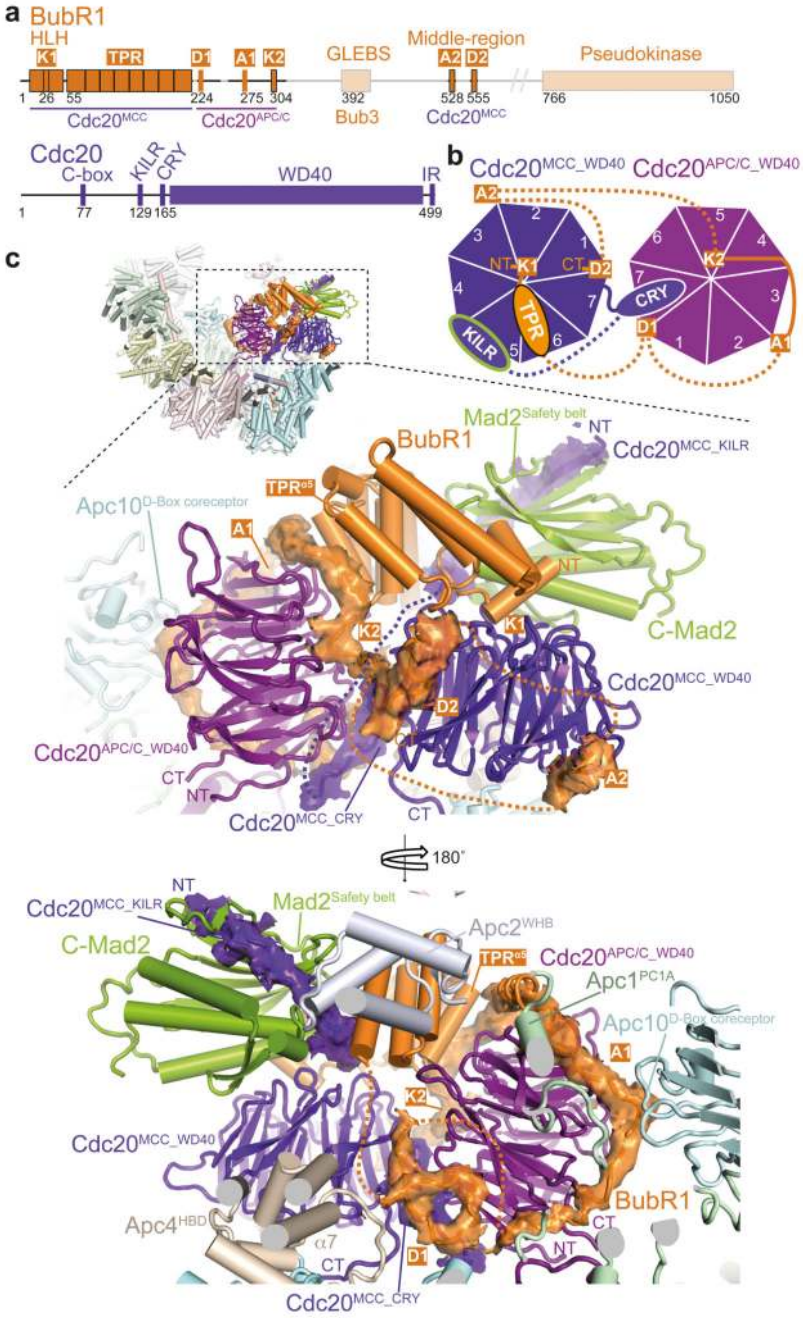

Figure 2. Interactions of BubR1 with Cdc20$^{APC/C}$ and Cdc20^{MCC}.

a, Schematic of BubR1 and Cdc20. **b**, Schematic representation of the top views of the Cdc20^{APC} and Cdc20^{MCC} WD40 domains. WD40 domain blades are numbered and the positions of BubR1 inhibitory degrons (orange) are indicated. The CRY degron 49 mediates Cdc20^{MCC} interactions with Cdc20$^{APC/C}$ (Extended Data Fig. 5f). **c**, Two views showing details of the MCC-Cdc20$^{APC/C}$ module. Cryo-EM density of the BubR1 inhibitory degrons, Cdc20^{MCC} CRY box and KILR motif is shown. Interactions of the BubR1 A1 motif with the

Apc10$^{D\text{-box coreceptor}}$ and Apc1; BubR1^{TPR} with Apc2^{WHB}; and Cdc20^{MCC} with Apc4^{HBD} are indicated (lower panel). Inset: overall view of APC/C^{MCC}.

Europe PMC Funders Author Manuscripts

Europe PMC Funders Author Manuscripts

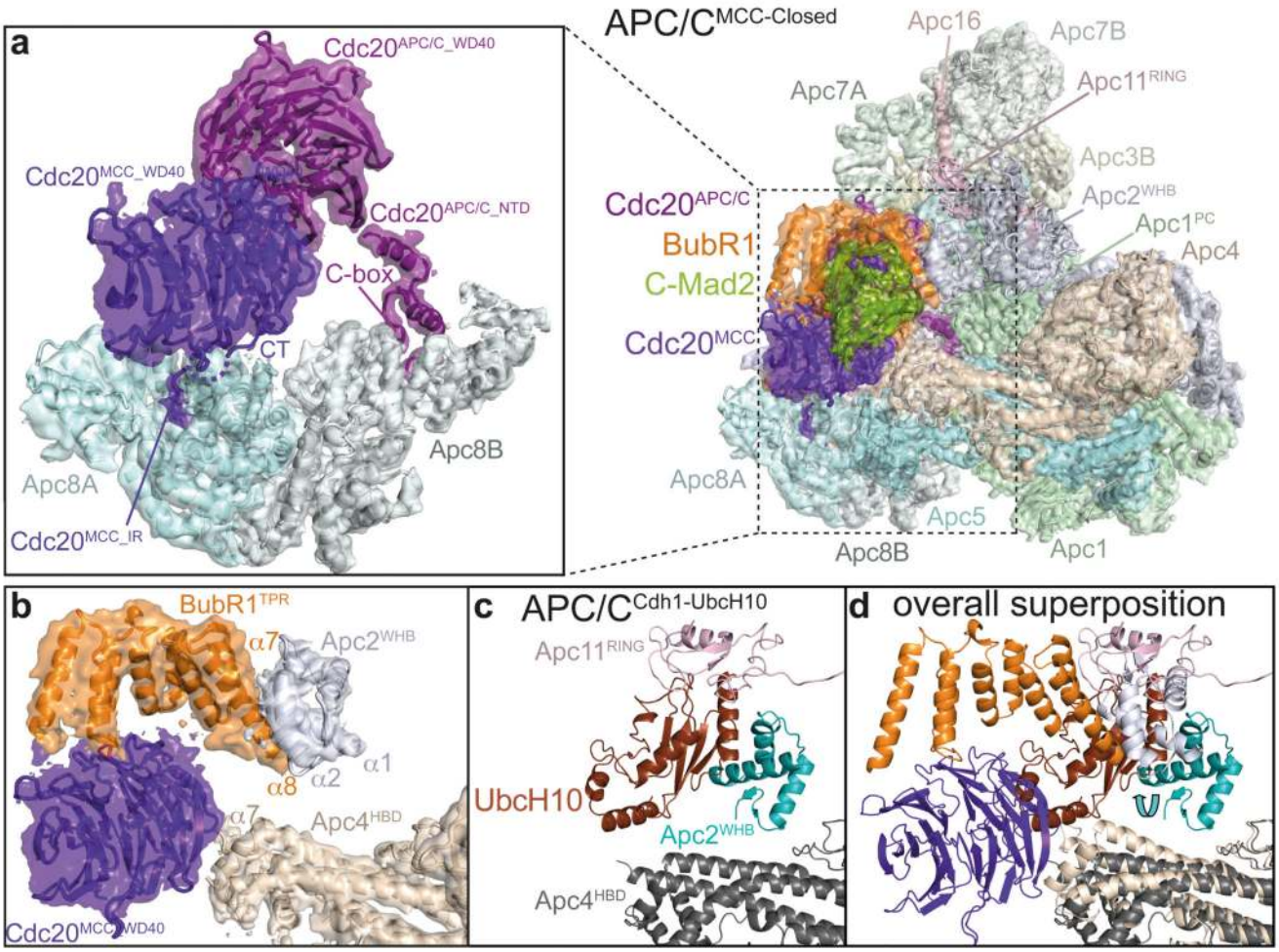

Figure 3. Interactions of the MCC-Cdc20$^{APC/C}$ module with the APC/C and APC/C catalytic inhibition by the MCC.

a, Right: an overview of the APC/C^{MCC} model with the corresponding cryo-EM density. Left: segmented cryo-EM density of the Apc8 dimer and its two associated Cdc20 molecules. Cdc20$^{APC/C}$ interacts with Apc8B via its N-terminal domain (NTD). Cdc20^{MCC} interacts with Apc8A through its C-terminal Ile Arg (IR) tail. **b, c, d**, Comparison of the binding mode of BubR1 and Cdc20^{MCC_WD40} in APC/C^{MCC} with the binding mode of UbcH10 in APC/C$^{Cdh1\text{-}UbcH10\text{-}Ub}$ (ref. 32). **b**, Segmented cryo-EM density of Cdc20^{MCC}, BubR1^{TPR}, Apc4^{HBD} and Apc2^{WHB}. (**c**) APC/C$^{Cdh1\text{-}UbcH10\text{-}Ub}$. (**d**) Both structures were superposed. BubR1^{TPR} and Cdc20^{MCC_WD40} compete for the same binding surfaces on Apc2^{WHB} and Apc4^{HBD} that form the UbcH10 binding site in APC/C$^{Cdh1\text{-}UbcH10\text{-}Ub}$ (Extended Data Fig. 5g). The Apc2^{WHB} sub-domain of Apc2 is shifted in the APC/C^{MCC} complex relative to APC/C$^{Cdh1\text{-}UbcH10\text{-}Ub}$ and would clash with the UbcH10-binding site on Apc11^{RING}.

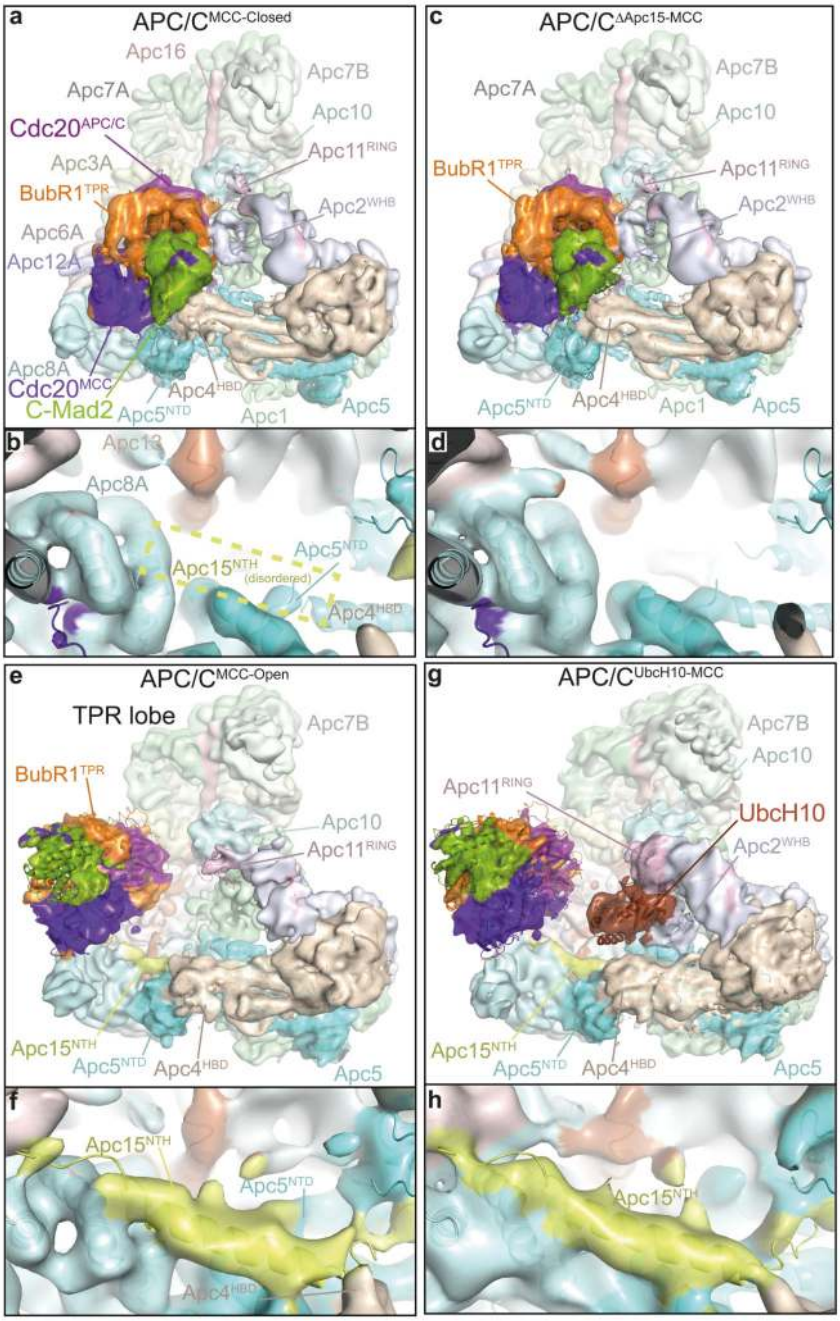

Figure 4. Cryo-EM structures of APC/C$^{MCC\text{-}Open}$, APC/C$^{\Delta Apc15\text{-}MCC}$, APC/C$^{UbcH10\text{-}MCC}$ and comparison with APC/C$^{MCC\text{-}Closed}$.

a, Top: overall view of the cryo-EM density of APC/C$^{MCC\text{-}Closed}$ and fitted coordinates for the MCC-Cdc20$^{APC/C}$ module, Apc2^{WHB} and Apc11. The APC/C^{MCC} subunits are coloured as in Figs 1 and 3. **b**, details of the Apc15^{NTH}-binding site on Apc8A and Apc5. Apc8A and Apc5 are shown. The position of the disordered Apc15^{NTH} is indicated by a box. **c, d**, APC/C$^{\Delta Apc15\text{-}MCC}$ (Apc15 deleted). **e, f**, APC/C$^{MCC\text{-}Open}$ and **g, h**, the APC/C$^{UbcH10\text{-}MCC}$ complex. Shown in (**a, b**), in APC/C$^{MCC\text{-}Closed}$, BubR1^{TPR} interacts with Apc2^{WHB}, and

Apc15^{NTH} is disordered. (**c, d**) In APC/C$^{\Delta Apc15\text{-}MCC}$ the MCC-Cdc20$^{APC/C}$ adopts the closed conformation, blocking the catalytic module. Conversely in APC/C$^{MCC\text{-}Open}$ (**e, f**) and APC/C$^{UbcH10\text{-}MCC}$ (**g, h**), BubR1^{TPR} no longer interacts with Apc2^{WHB}, and Apc15^{NTH} is ordered. (**g**) In APC/C$^{UbcH10\text{-}MCC}$, Apc2^{WHB} and Apc11^{RING} interact with UbcH10. All cryo-EM reconstructions were filtered to 8.5 Å.

Europe PMC Funders Author Manuscripts

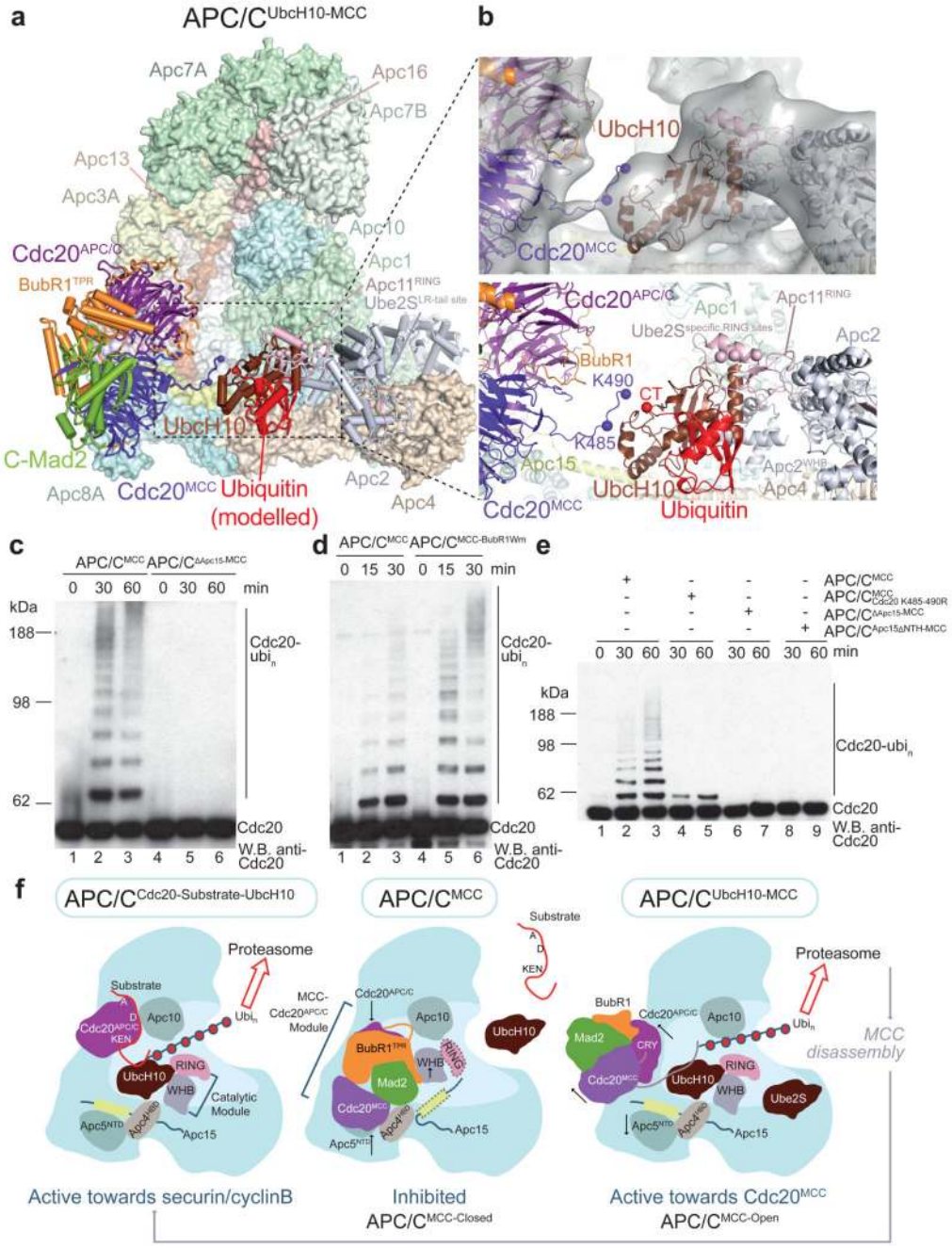

Figure 5. Mechanism of Cdc20 auto-ubiquitination by APC/C$^{UbcH10\text{-}MCC}$.

a, b, Model of a Cdc20^{MCC} ubiquitination complex based on the APC/C$^{UbcH10\text{-}MCC}$ cryo-EM reconstruction. The UbcH10-ubiquitin conjugate is modelled in the closed conformation 50. **b**, Top: cryo-EM density and model of APC/C$^{UbcH10\text{-}MCC}$. The EM map is filtered to 12 Å and displayed at slightly lower threshold than in Fig. 4g, see Extended Data Fig. 3e, for comparisons. Clear EM density connects Cdc20^{MCC} with UbcH10. Bottom: The Cdc20^{MCC} pre-ubiquitination model. Cdc20^{MCC} residues Lys485 and Lys490, ubiquitinated in logarithmic and checkpoint-arrested cells, respectively 30, are in close proximity to the

Europe PMC Funders Author Manuscripts

UbcH10 catalytic site (red sphere). **c**, Apc15 is required for Cdc20 ubiquitination by recombinant APC/C^{MCC}. **d**, $BubR1^{Wm}$ mutations at the $Apc2^{WHB}$ interface (R169A, F175A,V200A, L205) (Extended Data Fig. 5g) stimulates Cdc20 ubiquitination. **e**, Cdc20 residues Lys485 and Lys490 are ubiquitinated by recombinant APC/C^{MCC} (compare lanes 2,3 and 4,5). $Apc15^{NTH}$ is required for Cdc20 ubiquitination by recombinant APC/C^{MCC} (lanes 8,9). **f**, cartoon illustrating reciprocal regulation of APC/C and MCC by APC/C^{MCC}. In APC/$C^{MCC\text{-}Closed}$, MCC inhibits substrate (e.g. securin and cyclin B) and UbcH10 recognition. Cyclin A and Nek2A can bypass the SAC. In APC/$C^{MCC\text{-}Open}$, the UbcH10-binding site is exposed. Ube2S elongates Ub-conjugates initiated by UbcH10. Experiments in c-e were replicated three times. See Supplementary Fig. 1 for gel source data.